Molecular line mapping of the giant molecular cloud associated with RCW 106 - III. Multi-molecular line mapping

N. Lo,[1,2]⋆ M. R. Cunningham,[1] P. A. Jones,[1,3] I. Bains,[1,4] M. G. Burton,[1]
T. Wong,[1,2,5] E. Muller,[2,6]† C. Kramer,[7] V. Ossenkopf,[8,9] C. Henkel,[10]
G. Deragopian,[11] S. Donnelly[1] and E. F. Ladd[12]

[1]*School of Physics, University of New South Wales, Sydney, NSW 2052, Australia*
[2]*Australia Telescope National Facility, CSIRO, PO Box 76, Epping, NSW 1710, Australia*
[3]*Departamento de AstronomÃa, Universidad de Chile, Casilla 36-D, Santiago, Chile*
[4]*Centre for Astrophysics and Supercomputing, Swinburne University of Technology, P.O. Box 218, Hawthorn, VIC 3122, Australia*
[5]*Astronomy Department, University of Illinois, 1002 W. Green St, Urbana, IL 61801, USA*
[6]*Department of Astrophysics, Nagoya University, Furo-cho, Chikusa-ku, Nagoya 464-8602, Japan*
[7]*Instituto de Radioastronomia Milimetrica (IRAM), Avda. Divina Pastora 7, E-18012 Granada, Spain*
[8]*I. Physikalisches Institut, Universität zu Köln, Zülpicher Straße 77, 50937 Köln, Germany*
[9]*SRON, Netherlands Institute for Space Research, PO Box 800, 9700 AV Groningen, The Netherlands*
[10]*Max-Planck-Institut für Radioastronomie, Auf dem Hügel 69, 53121 Bonn, Germany*
[11]*Centre for Astronomy, James Cook University, Townsville, Australia*
[12]*Department of Physics and Astronomy, Bucknell University, Lewisburg PA 17837, USA*

ABSTRACT

We present multi-molecular line maps obtained with the Mopra Telescope towards the southern giant molecular cloud (GMC) complex G333, associated with the HII region RCW 106. We have characterised the GMC by decomposing the 3D data cubes with GAUSSCLUMPS, and investigated spatial correlations among different molecules with principal component analysis (PCA). We find no correlation between clump size and line width, but a strong correlation between emission luminosity and line width. PCA classifies molecules into high and low density tracers, and reveals that HCO^+ and N_2H^+ are anti-correlated.

Key words: stars: formation - ISM: clouds - ISM: molecules - ISM: structure - radio lines: ISM

1 INTRODUCTION

This is the third paper (paper I by Bains et al. 2006 and paper II by Wong et al. 2008) in a series of multi-molecular lines observations of the giant molecular cloud (GMC) associated with RCW 106, G333. The G333 giant molecular cloud, a southern massive star forming region, spans $1°.2 \times 0°.6$ on the sky, roughly centred on $l \sim 333°$, $b \sim -0°.5$ ($\alpha_{J2000} = 16^h21^m, \delta_{J2000} = -50^d30^m$), at a distance of 3.6 kpc (Lockman 1979). The aim of the multi-molecular line study was to investigate the relationship between the dynamics of the interstellar medium and star formation. Further investigation and analysis planned include power spectra to study the role of turbulence in the GMC, and searching for evidence of triggered star formation.

The G333 GMC has previously been studied in other wavelengths, for example in the far-infrared by Karnik et al. (2001) and the 1.2-mm dust continuum by Mookerjea et al. (2004). A search for water masers was carried out by Breen et al. (2007). There are also numerous works on specific regions in this GMC, such as RCW 106 (e.g. Rodgers, Campbell & Whiteoak 1960, Russeil et al. 2005) and G333.6−0.2, one of the brightest southern compact HII regions (e.g. Goss & Shaver 1970, Becklin et al. 1973, Storey et al. 1989, Colgan et al. 1993, Fujiyoshi et al. 1998, 2001, 2005 and 2006). However, to date, there has been no systematic, 3-mm multi-molecular line mapping of this GMC. This study demonstrates the full capability of the Mopra Telescope's[1] new digital filter bank,

---

⋆ E-mail: nlo@phys.unsw.edu.au
† Bolton Fellow, ATNF

[1] The Australia Telescope Mopra telescope is part of the Australia Telescope, which is funded by the Commonwealth of Aus-

Table 1. List of observed molecular transitions mapped in G333. The columns are: (1) molecule; (2) transition; (3) rest frequency (Lovas, Johnson & Snyder 1979); (4) upper energy levels from the Cologne Database for Molecular Spectroscopy (CDMS, Müller et al. 2001, 2005); (5) calculated critical density: unless specified, $n_{crit} = A_{ul}/\langle\sigma(v)v\rangle$ where A_{ul} is the Einstein A coefficient obtained from CDMS, $\langle\sigma(v)\rangle = 10^{-15}$ cm^2 is the collision cross section and v is the velocity of collision particles assumed to be 1 km s^{-1}; (6) observation season; (7) backend used, where MPCOR stands for Mopra Correlator, which was decommissioned in 2005 and replaced with a new digital filter bank, the UNSW-Mopra Spectrometer (UNSW-MOPS); (8) notes, where [hf] denotes hyperfine structures, with the rest frequency quoted being that of the strongest hyperfine component, and [†] denotes molecules that have detectable emission at a few places only. Their emission maps are not presented in this work but will appear in subsequent papers on specific regions in the G333 cloud.

Molecule	Transition	Rest frequency (GHz)	E_u/k (K)	n_{crit} (cm^{-3})	Observation season	Backend	Notes
^{13}CO	$1-0$	110201.353	5.29	3×10^3	2004	MPCOR	
C^{18}O	$1-0$	109782.173	5.27	3×10^3	Jul, 2005	MPCOR	
C$_2$H	$1-0$	87316.925	4.19	2×10^5	Jul, 2006	MOPS	[hf]
CH$_3$OH	$2(0,2) - 1(0,1)\,A+$	96741.377	6.97	7×10^3	Sep, 2006	MOPS	[†]
CS	$2-1$	97980.953	7.05	2×10^5	Sep, 2006	MOPS	
C^{34}S	$2-1$	96412.961	6.94	2×10^5	Sep, 2006	MOPS	[†]
HCN	$1-0$	88631.847	4.25	2×10^5	Jul, 2006	MOPS	[hf]
H^{13}CN	$1-0$	86340.167	4.14	2×10^5	Jul, 2006	MOPS	[hf,†]
HCCCN	$10-9$	90978.989	24.01	6×10^5	Sep, 2006	MOPS	[†]
HCCCN	$11-10$	100076.385	28.82	8×10^5	Sep, 2006	MOPS	[†]
HCO$^+$	$1-0$	89188.526	4.28	4×10^5	Jul, 2006	MOPS	
H^{13}CO$^+$	$1-0$	86754.330	4.16	4×10^5	Jul, 2006	MOPS	[†]
HNC	$1-0$	90663.572	4.35	3×10^5	Jul, 2006	MOPS	[hf]
N$_2$H$^+$	$1-0$	93173.480	4.47	4×10^5	Sep, 2006	MOPS	[hf]
SiO	$2-1\,\nu=0$	86847.010	6.25	3×10^5	Jul, 2006	MOPS	[†]
SO	$3(2) - 2(1)$	99299.905	9.23	1×10^5	Sep, 2006	MOPS	[†]
	$4(5) - 4(4)$	100029.565	38.58	3×10^{7a}	Sep, 2006	MOPS	[†]

^{a} Ungerechts et al. (1997)

the UNSW-Mopra Spectrometer (UNSW-MOPS). Other similar surveys utilising the UNSW-MOPS are the H$_2$O Southern Galactic Plane Survey (HOPS) by Walsh et al. (2008) and the Central Molecular Zone of the Galaxy by Jones et al. (2008).

We present in this paper results of molecular line mapping carried out during July to November in 2006, consisting of molecular lines from 83 to 101 GHz. For a detailed analysis of ^{13}CO and C^{18}O data please refer to previous work by Bains et al. (2006, hereafter BWC2006) and Wong et al. (2008, hereafter WLB2008). In Section 2 we describe the observing technique, and the new UNSW-MOPS digital filter bank. In Section 3 we present the results, and examine the velocity and spatial distribution of the molecular emission from the different molecules. In Section 4 and 5, we present two different approaches to characterising emission distribution in the GMC: Clump finding with GAUSSCLUMPS and principal component analysis (PCA). In Section 6 we discuss results, including specific regions of the GMC. Finally, we summarise our findings in Section 7.

Data presented here will be made available in the near future, please contact the authors for details.

tralia for operation as a National Facility managed by CSIRO (ATNF, http://www.atnf.csiro.au).

2 OBSERVATIONS

The data were collected with the 22 metre Mopra Telescope, which is a centimetre- and millimetre-wavelength antenna having a full width to half-maximum (FWHM) beam size of $\sim 36''$ at 100-GHz (Ladd et al. 2005). The observations were carried out with the narrow band mode of the new UNSW-Mopra Spectrometer (UNSW-MOPS) digital filterbank back-end, and a Monolithic Microwave Integrated Circuit (MMIC) 77 to 116 GHz receiver. The observing parameters, including rest frequencies and dates are listed in Table 1. UNSW-MOPS has a 8-GHz bandwidth with four overlapping 2.2-GHz subbands, each subband having four dual-polarisation 137.5-MHz-wide windows giving a total of sixteen dual-polarisation windows. Each window has 4096 channels providing a velocity resolution of ~ 0.1 km s^{-1} per channel at 100 GHz. The velocities presented in this work are with respect to the kinematic local standard of rest (LSR), with $v_{\rm LSR} = -50$ km s^{-1} being the systemic velocity of the G333 complex.

The brightness temperature $T_{\rm b}$ is related to the antenna temperature $T_{\rm A}^*$ by $T_{\rm b} = T_{\rm A}^*/\eta_\nu$, where η_ν is the frequency dependent beam efficiency. According to Ladd et al. (2005) the main beam efficiency at 86 GHz is $\eta_{86\,{\rm GHz}} = 0.49$, and at 110 GHz is $\eta_{110\,{\rm GHz}} = 0.44$. The beam efficiencies are $\eta_{86\,{\rm GHz}} = 0.65$ and $\eta_{86\,{\rm GHz}} = 0.56$ at 86 and 110 GHz respectively. The results presented in this paper are in terms of antenna temperature $T_{\rm A}^*$ unless otherwise specified.

We followed a similar mapping procedure to our previous work (^{13}CO; BWC2006). The ~ 1 square degree region was divided into 300 $\times$ 300 square arcsec fields,

with pointing centres separated by 285 arcsec in right ascension and declination, allowing a 15-arcsec overlap between adjacent fields. Each field was mapped with two passes, the first pass scanning in right ascension and the second pass scanning in declination. The observing mode was 'on-the-fly'(OTF) raster scanning, at a scan rate of 3.5 arcsec s^{-1} and averaging data over a 2-s cycle time. We used the ^{13}CO map as a guide, mapping the brightest ^{13}CO fields first, then extending these to cover the majority of the emission in most detected molecules, resulting in maps covering $\sim$0.7 square degrees. We used two frequency settings centred at 87 and 97 GHz, with each setting covering an 8-GHz bandwidth, 4-GHz on either side of the central frequency.

We have used the SiO masers IRSV1540 and AH Scorpii for pointing calibration. Pointing calibration was performed at the beginning of each map, therefore approximately every 50 minutes. Estimated pointing errors are within 10 arcseconds.

At the end of each day's observation, a 5 minute position switched observation of M17SW was carried out with the same frequency settings as for the maps, to monitor the performance of the system. Based on these observations the deviation of T$_A^*$ during the whole observing season is within 10 per cent.

The data were reduced with the LIVEDATA and GRIDZILLA packages available from the ATNF, written by Mark Calabretta[2]. LIVEDATA performs a bandpass calibration using the preceding reference (off-source) scan, then fits the spectral baseline with a first degree polynomial. Due to low sensitivity near the start and end of the window, the first and last 750 channels were discarded before baseline fitting. GRIDZILLA grids the data according to user specified weighting and beam parameter inputs. In this work, our data was weighted by the relevant system temperature (T$_{sys}$) and Gaussian smoothed during data reduction stage. The data cubes were gridded with three pixels across each beam width, therefore each pixel is $\sim 15 \times 15$ arcsec^2 for data with 87-GHz frequency setting, and $\sim 12 \times 12$ arcsec^2 for the 97-GHz setting. Note that all data cubes presented in this work are regridded to 15×15 arcsec^2 pixel size for ease of comparison, and the velocity resolution is left as ~ 0.1 km s^{-1}.

3 RESULTS

3.1 Spatial distribution of the molecules

Different molecules may trace different physical conditions within the region, such as density, chemistry, temperature, evolutionary stage, and so on. Our selection of molecules covers those which may trace differences in density, temperature and dynamic features such as outflow, allowing us to study environmental varieties within this giant molecular cloud. Since some molecules (e.g. CH$_3$OH, HCCCN) have detectable emission at a few places only, their emission maps and velocity profiles are not presented here, but in subsequent works focusing on specific regions.

Table 2. A list of the emission range, peak brightness and 1σ level of the integrated emission maps shown in Figures 1 and 2.

Molecule	Emission range (km s^{-1})	1σ (K km s^{-1})	Peak brightness (K km s^{-1})
^{13}CO	-70 to -40	0.3	95
C^{18}O	-70 to -40	0.2	19
CS	-70 to -40	0.2	30
HCO$^+$	-70 to -40	0.1	21
HCN	-80 to -30	0.1	21
HNC	-70 to -40	0.1	18
N$_2$H$^+$	-80 to -30	0.2	11
C$_2$H	-60 to -40	0.2	5

Shown in Figure 1 and 2 are the integrated intensity (zeroth moment) maps of the observed molecular lines (contours) overlaid on the *Spitzer* Galactic Legacy Infrared Midplane Survey Extraordinaire (GLIMPSE; Benjamin et al. 2003) 8.0-μm image (grey scale). The integrated velocity range is -70 to -40 km s^{-1} for ^{13}CO (BWC2006), C^{18}O (WLB2008), CS, HCO$^+$ and HNC, and -60 to -40 km s^{-1} for C$_2$H. A wider velocity range was chosen for molecules with hyperfine components: -80 to -30 km s^{-1} for HCN and N$_2$H$^+$, so as to include emission from all components. The choice of velocity range reflects emission from the GMC only. Emission outside this range comes from spiral arms and intermittent clouds. The maps were Gaussian smoothed with an FWHM of 45 arcsec. The labels in the ^{13}CO total intensity map (Figure 1a) indicate some of the molecular regions in proximity to bright HII regions and *IRAS* sources, as marked by rectangles. The starting contour levels are based on the lowest detectable emission above noise, hence outlining the emission structure of the cloud. Note that contours near the edges of the maps are noisy; this is because the edges were scanned with one pass only and thus have lower sensitivity. Details of the integrated emission maps are summarised in Table 2.

The CS total intensity map (Figure 1c) shows a more confined distribution than the ^{13}CO emission. This is as expected from a dense gas tracer such as CS, with a critical density of $\sim 10^5$ cm^{-3}. However CS has a similar distribution to another CO isotope presented here $-$ C^{18}O. HCO$^+$ (Figure 1d), a common ionic species found in molecular clouds also presents a similar distribution to CS, as do HCN (Figure 2a) and HNC (Figure 2b).

A comparison of HCN and HNC total intensity maps (Figures 2a and b), shows that they both have similar distributions in general. This is surprising because of the strong chemical differences between HCN and HNC, meaning that its abundance ratio can depend heavily on, for example, temperature (e.g. Schilke et al. 1992; Hirota et al. 1998). We do note there are local variations where temperature changes, such as the massive dense cold core where HCN and HNC have different spatial distribution (Lo et al. 2007).

The total emission map of N$_2$H$^+$ (Figure 2c) shows that this molecule has a more compact and clumpier distribution than other molecules. It also shows regions with intense N$_2$H$^+$ emission which show diffuse emission in other molecules; here we highlight two such regions on the map (indicated by arrows). The source G333.125$-$0.56 (bottom arrow) is a massive dense cold core, with temperatures of
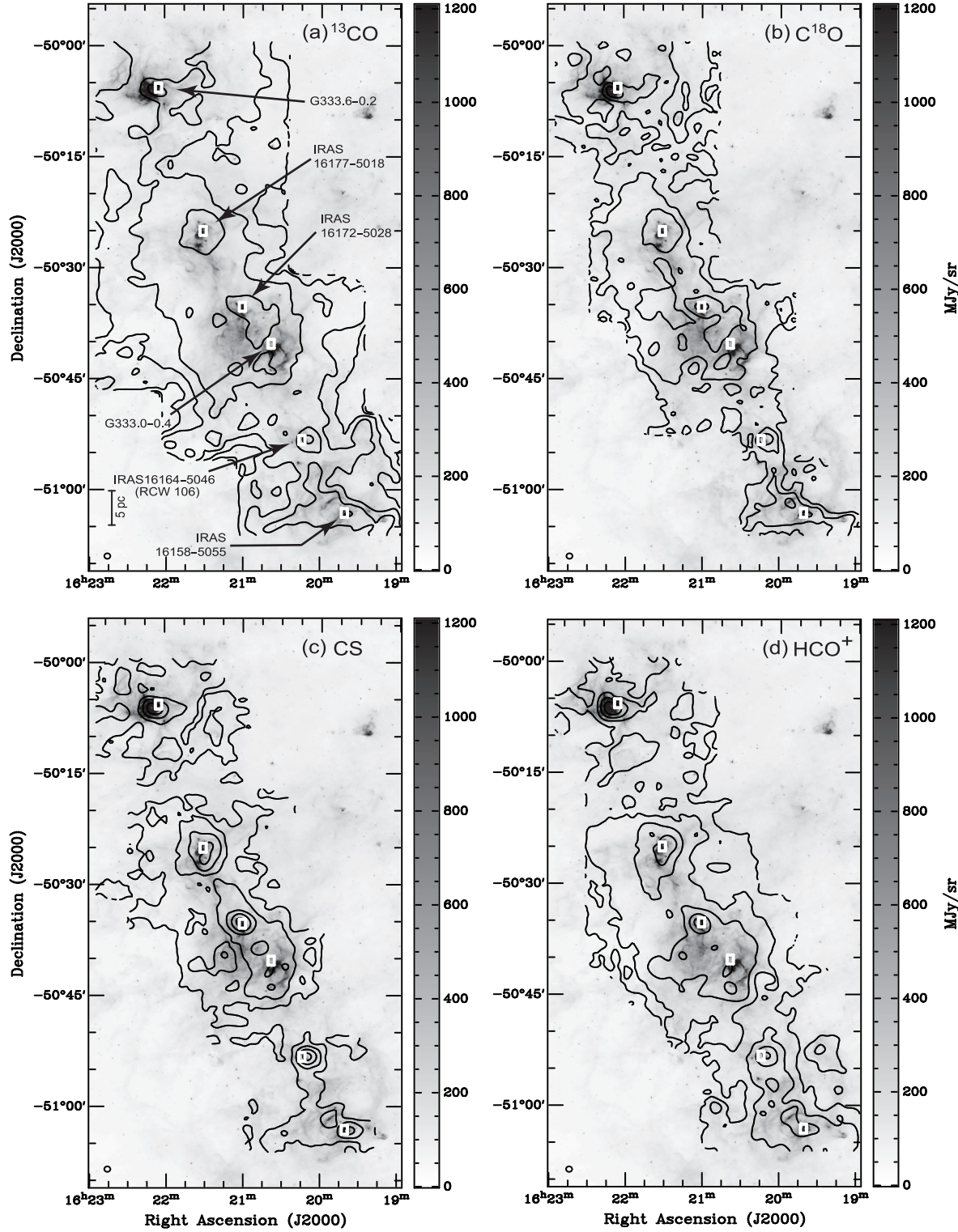
Figure 1. Integrated emission maps (contours) for ^{13}CO ($J = 1 - 0$), C^{18}O ($J = 1 - 0$), CS ($J = 2 - 1$) and HCO$^+$ ($J = 1 - 0$) overlaid on a *Spitzer* IRAC 8.0-μm image (grey scale). The maps are integrated over a velocity range of -70 to -40 km s^{-1} and were clipped at a 3 σ level. 1 σ is 0.3 K km s^{-1} for ^{13}CO, 0.2 K km s^{-1} for C^{18}O and CS, and 0.1 K km s^{-1} for HCO$^+$. The maps were then Gaussian smoothed with an FWHM of 45 arcsec. The contour levels start at 1.5 K km s^{-1} for ^{13}CO, 2.0 K km s^{-1} for C^{18}O, 1.4 K km s^{-1} for CS and 1.0 K km s^{-1} for HCO$^+$. Then each successive contour level is double the value of the previous one. The choice of lowest contour level is based on the lowest detectable emission above noise, except for ^{13}CO where there is emission detected throughout the map. The temperatures are in terms of the antenna temperature, T_A^*. Previously designated H\,\textsc{ii} regions and the associated *IRAS* sources are marked with white rectangles and names are shown in the ^{13}CO map. The scale bar shown in the ^{13}CO map indicates 5-pc at a distance of 3.6-kpc and the tiny circle in the lower left corner of each panel show the FWHM beam size after smoothing. The velocity range used here reflects emission from the GMC only; emission outside this range comes from more distant spiral arms or intervening clouds.
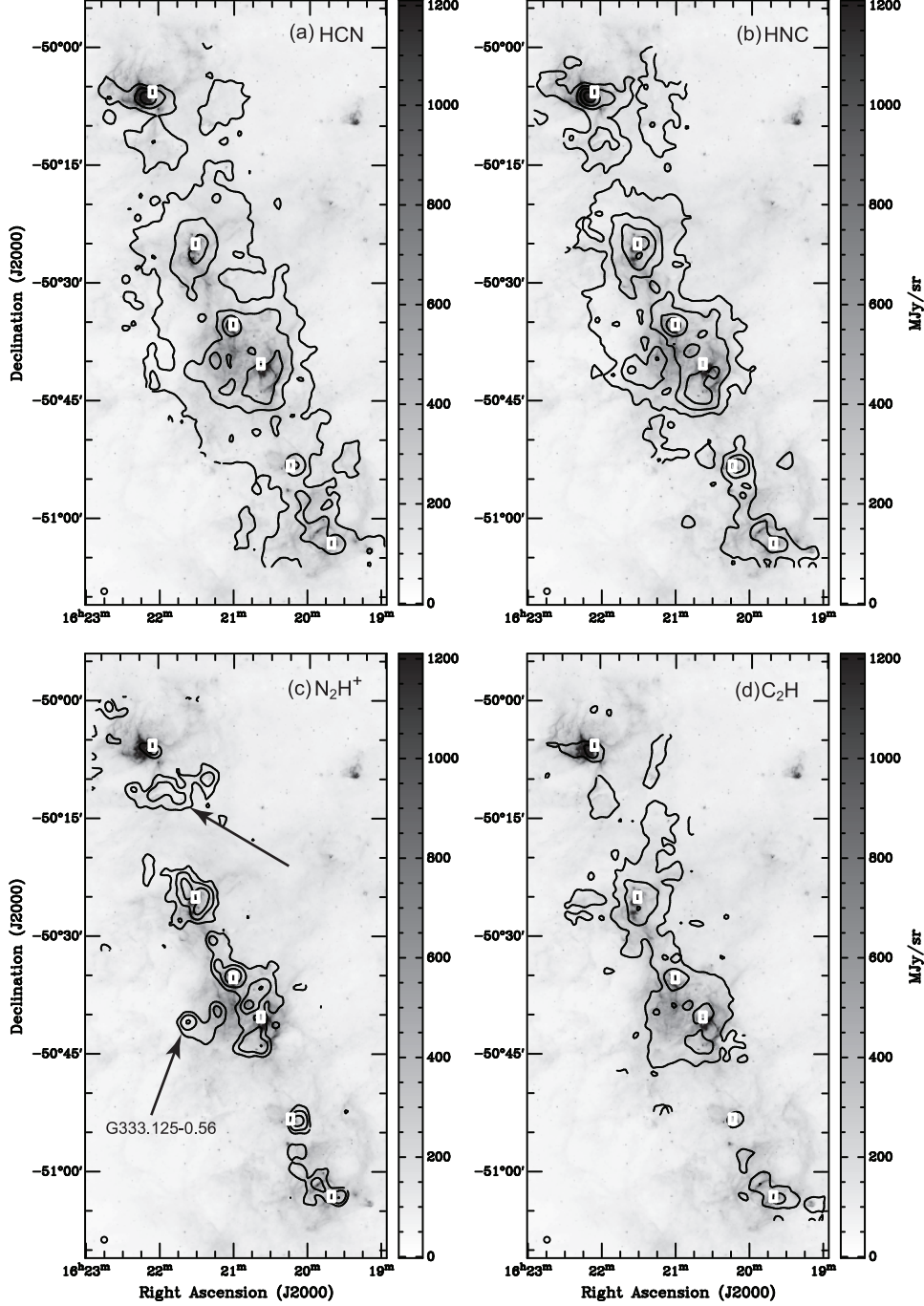
Figure 2. Integrated emission maps (contours) for HCN ($J = 1 - 0$), HNC ($J = 1 - 0$), N_2H^+ ($J = 1 - 0$) and C_2H ($J = 1 - 0$) overlaid on *Spitzer* IRAC 8-μm images (grey scale). The integrated velocity ranges are of -80 to -30 km s^{-1} for HCN and N_2H^+, -70 to -40 km s^{-1} for HNC and -60 to -40 km s^{-1} for C_2H. The maps were clipped at a 3 σ level. 1 σ is 0.1 K km s^{-1} for HCN and HNC, and 0.2 K km s^{-1} for N_2H^+ and C_2H. The maps were then Gaussian smoothed with an FWHM of 45 arcsec. The contour levels start at 2.0 K km s^{-1} for HCN, 1.3 K km s^{-1} for HNC, 1.6 K km s^{-1} for N_2H^+ and 1.2 K km s^{-1} for C_2H, then each successive level is double the previous one. The choice of lowest contour levels are based on the lowest detectable emission above noise. The temperatures are in terms of T_A^* and the tiny circle in the lower left corner of each panel show the FWHM beam size after smoothing. Previously designated H II regions and the associated *IRAS* sources are marked with white rectangles (see Figure 1 for their naming). The arrows indicate two N_2H^+ emission peaks, which are not prominent in other emission maps. Note that the differences in velocity range between molecules are due to hyperfine splitting such that some molecules have a wider velocity distribution. The velocity range used here reflects emission from the GMC only; emission outside this range is from more distant spiral arms or intervening clouds.

13 to 19 K derived from the NH_3 (J,K) = (1,1) and (2,2) inversion line and from the spectral energy distribution (SED). It has broad thermal SiO emission, and is believed to be a deeply embedded young stellar object in an early stage of star formation (Lo et al. 2007). In the northern part of the map, the N_2H^+ emission indicated by the top arrow is similarly interesting. Here, bright N_2H^+ emission is detected where other molecules show diffuse weak emission. A comparison with the GLIMPSE 8.0-μm image clearly shows that N_2H^+ aligns well with the infrared dark filaments, as discussed later in Section 6.3. While N_2H^+ seems to be correlated with infrared dark filaments, C_2H does the opposite; it seems to correlate with GLIMPSE 8.0-μm emission.

Among the eight molecules we present, C_2H emission is the weakest. Its spatial distribution is more extended than the quiescent gas tracer N_2H^+, but not as extended as other molecules.

3.2   Velocity distribution of the molecules

Spatially averaged spectral emission profiles of the molecules presented in Section 3.1 are shown in Figure 3. Note that the apparent lower signal-to-noise of the N_2H^+ and C_2H spectra is due to these two molecules being less extended spatially. To illustrate this, spectra of specific regions (IRAS16172−5028, IRAS16164−5046 and G333.125−0.56) are shown in Figure 4, showing that the signal-to-noise level is comparable among the molecular lines. From the spectral profiles in Figure 3 we can see that the molecular emission peaks at ~ -50 km s^{-1}, the systemic velocity of the G333 cloud, and spans a velocity range of ~ -70 to ~ -40 km s^{-1}. ^{13}CO, $C^{18}O$ and CS have similar velocity structure, such as the emission 'shoulders' at ~ -40 and ~ -55 km s^{-1}. The ~ -55 km s^{-1} emission feature also appears in the HCO^+ and HNC profiles. HCN and N_2H^+ have the widest velocity range, but this is due to hyperfine splitting rather than actual differences in distribution. The ^{13}CO velocity feature centred at -70 km s^{-1} comes from a different cloud along line of sight, as discussed in BWC2006.

From the ^{13}CO data, BWC2006 noted a linear velocity gradient of ~ 0.2 km s^{-1} pc^{-1} across the GMC (1 arcmin is 1 pc for this GMC at distance of 3.6 kpc), which is five times larger than the velocity gradient due to Galactic rotation (~ 0.04 km s^{-1} pc^{-1} for an angular separation of $\sim$65 arcmin at $b = 333°$, see BWC2006). To investigate whether molecules other than ^{13}CO are involved in this bulk gas motion, we plotted the position-velocity (pv) map of CS, HCO^+, HNC and C_2H across the GMC as shown in Figure 5. The pv slice is positioned such that it cuts through the major emission ridge of the GMC, as shown in the top panel inset. The centre position (zero angular offset) is roughly at $\alpha_{J2000} = 16^h21^m$, $\delta_{J2000} = -50^d30^m$ near IRAS16172−5028, with positive offset corresponding to the southern part of the GMC.

Evident in the CS pv map are a number of emission clumps; those near the GMC centre (centred on 0' offset) are surrounded by diffuse gas. The line widths of these emission clumps are ~ 4 to 14 km s^{-1}. Similar to ^{13}CO, the velocity gradient is also noticeable in CS, HCO^+, HNC and C_2H, ~ 10 km s^{-1} over roughly 50 arcmin (~ 0.2 km

s^{-1} pc^{-1}), comparable to that of the ^{13}CO. The HCO^+ pv map shows similar overall structure to CS in general, however the centre velocity of the strong emission clump at -30 arcmin (G333.6−0.2, as labelled in Figure 5) is -50 km s^{-1} for HCO^+, compared to -48 km s^{-1} for CS, with HCO^+ emission being more extended towards the negative velocities (~ -60 km s^{-1}) than CS. Where the CS emission clump peaks at -48 km s^{-1}, the HCO^+ emission clump is less intense and appears to host two components. In the HNC emission, the structure of this feature is consistent with CS. In the 3-D data cube, the HCO^+ spectrum shows a deep self-absorption feature at this position, when compared with the optically thin $H^{13}CO^+$, explaining the absence of HCO^+ emission. In general, the HNC and C_2H pv maps show a similar velocity structure to CS, except there is no detectable C_2H at ~ 28 arcmin at -58 km s^{-1}.

In the next two sections, we will present two different approaches in characterising the distribution of the emission in the GMC, clump finding with GAUSSCLUMPS and principal component analysis.

4   CLUMP ANALYSIS

One of the aims of this multi-molecular line mapping is to examine how different molecules correlate with each other in the GMC. To characterise the distribution of molecules, we have used the Gaussian clump decomposition algorithm GAUSSCLUMPS (Stutzki & Guesten 1990; Kramer et al. 1998) to decompose the observed three-dimensional data cubes into individual 'clumps' of emission. There has been some discussion in recent years about the best type of automatic clump decomposition algorithm to use in giant molecular clouds (see Sheth et al. 2008 for a good discussion on this subject). GAUSSCLUMPS and CLUMPFIND (Williams, de Geus & Blitz 1994) are algorithms which work by identifying peak pixels within a data cube or image, and then identifying other nearby pixels which may be part of the same clump. CLUMPFIND stops adding pixels to a clump when it reaches pixels below a user specified contour level (see BWC2006 for a more lengthy discussion of this algorithm). GAUSSCLUMPS decomposes the data cube by iteratively fitting the peak position as a Gaussian distribution, then subtracting the fitted clumps and fitting the residual map. Both these methods have the disadvantage that they tend to break the emission into many small clumps close to the resolution element of the data set, particularly with a low signal-to-noise data set. Rosolowsky & Leroy (2006) have described a different method, implemented by the algorithm CPROPS, which uses a combination of moments and principal component analysis to identify clumps in data cubes, which they find is more robust against the effects of resolution and noise. However, of the three methods, we find GAUSSCLUMPS provided the best set of physically plausible clumps for the molecular transitions presented in this paper, which trace dense confined gas, with CPROPS finding very few clumps in each data cube. This is consistent with the finding of Rosolowsky & Leroy (2006) that GAUSSCLUMPS is the most effective algorithm for separating tight blends of clouds. Consequently, we have chosen to use the GAUSSCLUMPS
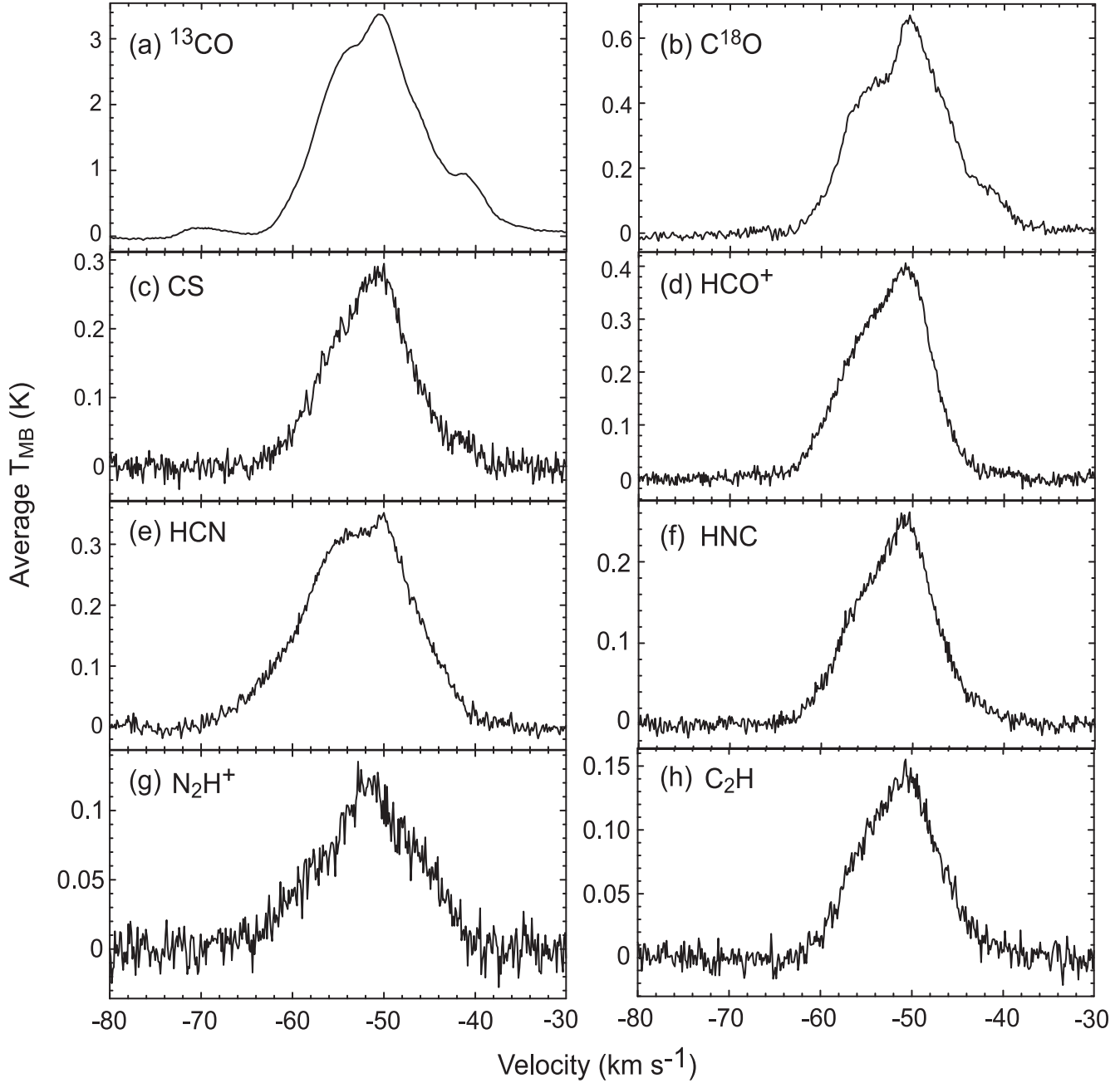
Figure 3. Spatially averaged emission profiles of the whole GMC. The temperatures are in terms of T_A^*. Note that the lower signal-to-noise ratio of the N_2H^+ and C_2H spectra is due to these two molecules being less extended spatially; the 1 σ level is comparable to other more extended molecules.

algorithm, but have also undertaken a careful check of the clumps produced to confirm that they are physically plausible.

The molecules selected for such clump finding are CS, HCO^+, HNC and C_2H. The selection is based on CS and HCO^+ emission not having hyperfine splitting, HNC hyperfine splitting not being resolvable, and the C_2H hyperfine component separation being so wide that only one component falls into the velocity range. The data cubes were smoothed with a hanning window width of five channels and binning window of two channels, giving a velocity resolution of $\sim$ 0.3 km s^{-1}, to improve the signal-to-noise ratio. The rms levels after binning are 0.070, 0.065, 0.06 and 0.06 K (in antenna temperature, T_A^*) per 0.3 km s^{-1} for CS, HCO^+, HNC and C_2H respectively. We have set the intensity threshold at the 5σ level, therefore clumps with peak temperature below 5σ are discarded for CS, HCO^+ and HNC. For C_2H, due to its comparatively weak emission, we only discarded clumps with peak temperature below the 3σ level. For all molecules the spectral line emission towards the clumps was examined to confirm that the emission is real. We also excluded clumps that have angular sizes smaller than 1.5 beam-widths to reduce the number of false detections. Clumps that are
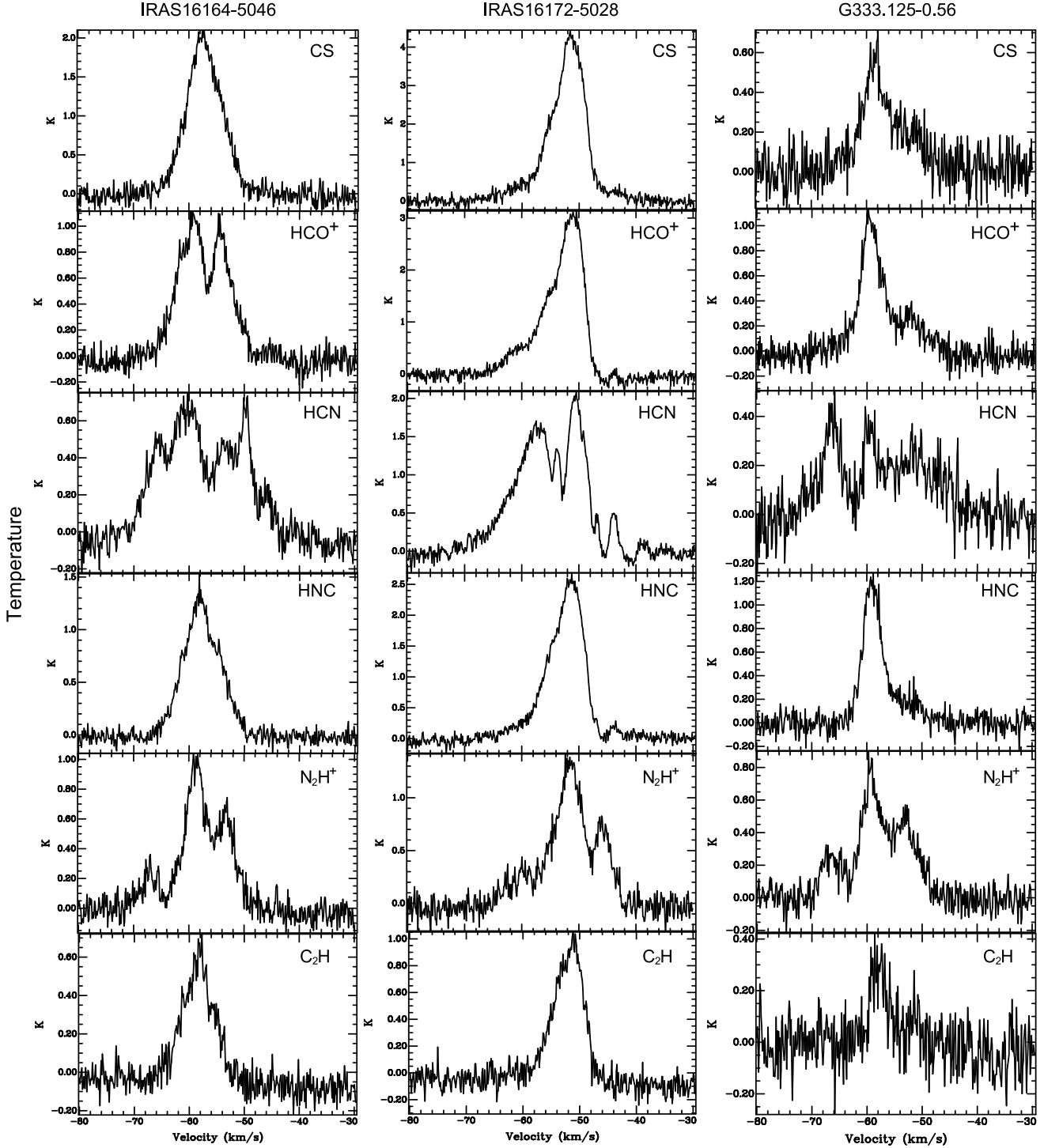
Figure 4. Sample spectra towards two of the IRAS sources (IRAS16172−5028 and IRAS16164−5046) and the cold core G333.125−0.56 in G333, showing the general quality of the data, and the consistent noise level within the data set. Line temperatures are given on a T_A^* scale.

found on the edges of the maps are also discarded, due to the lower sensitivity as the map edges contain one pass only.

4.1   Clump properties

GAUSSCLUMPS finds 129, 186, 128 and 78 clumps in the CS, HCO$^+$, HNC and C$_2$H data cubes, respectively. GAUSSCLUMPS reports centre positions and velocities, line widths, angular sizes, peak temperatures and internal velocity gradients of the identified clumps. We have listed
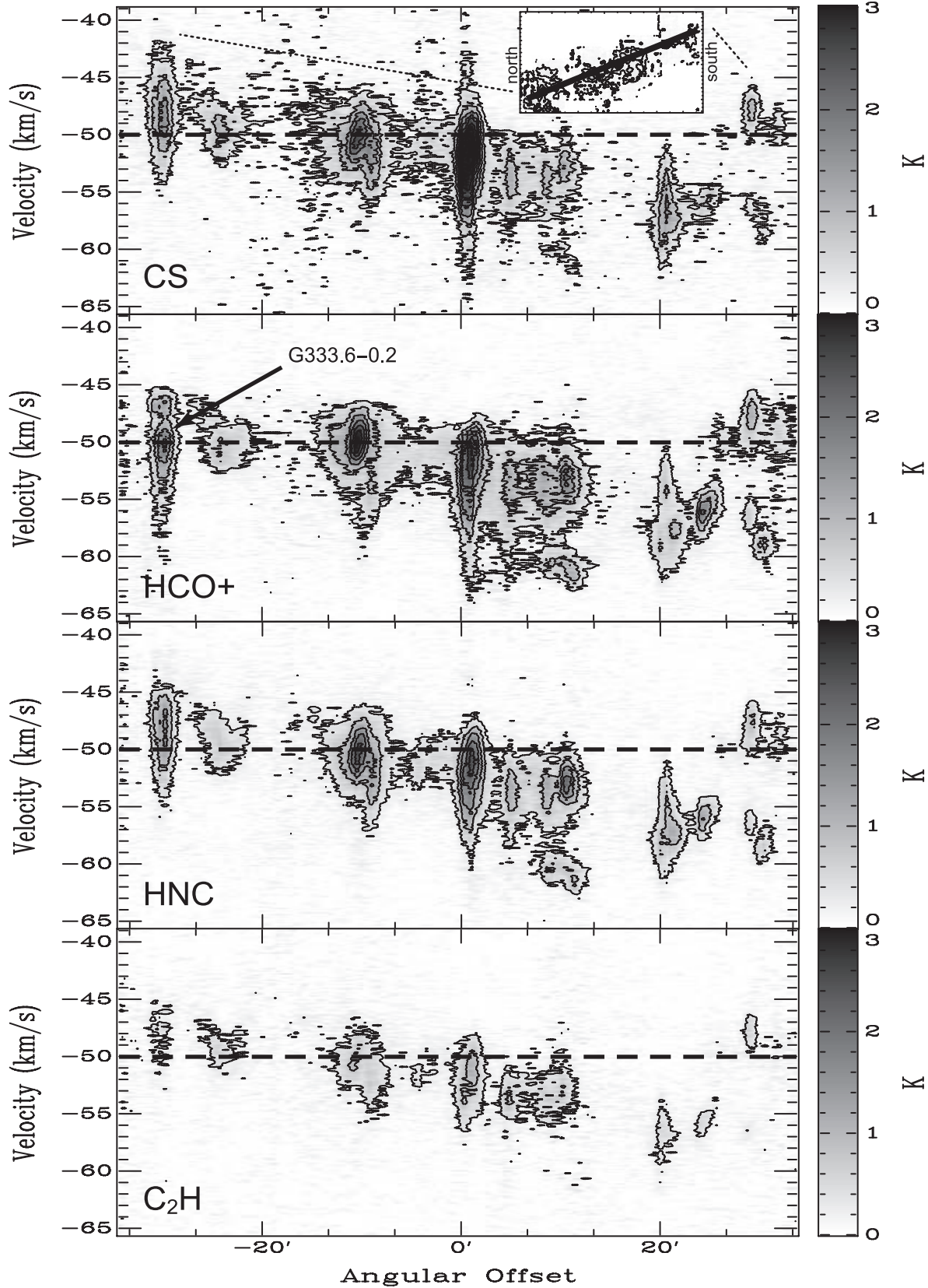
Figure 5. Position-velocity diagrams of CS, HCO$^+$, HNC and C$_2$H centred at approximately $\alpha_{J2000} = 16^h21^m$, $\delta_{J2000} = -50^d30^m$. The inset in the top panel shows the position-velocity cut presented in the diagrams. The contour levels all start at the 3σ level, 0.3 K, increasing to 3.0 K with increments of 0.5 K. The temperatures are in terms of T_A^*. Positive angular offset corresponds to the southern region of the GMC. The arrow points toward the H II region G333.6−0.2.

Table 3. The 20 brightest CS clumps selected according to decreasing peak temperature with line intensities above the 5σ level of the Hanning smoothed data cube. Also in Tables 4, 5 and 6: The listed properties are centre position (RA and Dec), centre velocity (v in km s^{-1}), full width to half maximum (FWHM) line width (ΔV in km s^{-1}), FWHM of the two principal axes (D_x and D_y in arcmin), peak temperature ($T_b = T_A^*/\eta_\nu$ in K), internal velocity gradient across the clump (dv/dr in km s^{-1} arcmin^{-1}), calculated luminosity (L in K km s^{-1} pc^2), $L = (d\,[\mathrm{pc}])^2 (\frac{\pi}{180\times3600})^2 (r_x r_y) \int T_b \delta v$ (see text for details) and associated clumps in other molecules. See the online version for a complete list of 129 clumps.

#	RA	Dec	v	ΔV	D_x	D_y	Peak T_b	dv/dr	L	Associated clumps in other molecules
CS01	16:21:02.0	-50:35:04.9	-52.2	2.8	1.7	1.4	7.6	0.4	48.7	HCOp02, HNC02, C2H01
CS02	16:21:01.3	-50:35:22.9	-49.5	2.5	1.6	1.6	5.2	0.1	33.4	HCOp02, HNC02, HNC05, C2H01
CS03	16:22:07.8	-50:06:22.9	-47.8	4.1	2.0	1.3	4.9	0.4	49.1	CS14, HCOp03, HCOp09, HNC01, HNC10
CS04	16:21:02.0	-50:34:58.9	-55.3	3.1	1.0	1.2	4.4	0.1	14.8	HCOp05, C2H05
CS05	16:20:10.2	-50:53:16.9	-57.4	3.4	1.5	1.6	3.8	0.8	29.8	CS09, CS15, HCOp18, HNC11, HNC17, C2H06
CS06	16:21:27.1	-50:24:52.9	-50.4	2.6	1.9	2.4	3.6	0.2	42.2	HCOp03, HNC03, C2H08
CS07	16:21:30.3	-50:26:46.9	-52.2	3.2	1.4	1.7	3.6	0.2	26.7	CS16, HCOp16, HCOp20, HNC12, C2H02
CS08	16:21:13.3	-50:39:46.9	-55.6	2.0	1.3	1.7	2.9	0.5	12.4	CS17, HCOp07, HNC07, C2H07
CS09	16:20:11.5	-50:53:22.9	-54.2	3.2	1.1	0.9	2.6	0.5	8.1	CS05, HCOp18, HNC17
CS10	16:20:26.0	-50:41:22.9	-56.0	2.4	1.2	1.4	2.6	0.3	9.9	HCOp14, HNC16, C2H11
CS11	16:20:46.9	-50:38:46.9	-53.3	2.6	1.4	1.2	2.5	0.3	10.4	HNC18, C2H04
CS12	16:21:37.8	-50:24:52.9	-50.8	3.0	1.1	2.4	2.0	0.5	16.1	C2H15
CS13	16:19:37.1	-51:03:28.9	-50.6	3.7	1.7	1.2	2.0	0.7	14.6	C2H12
CS14	16:22:07.8	-50:06:04.9	-45.3	2.0	1.7	1.4	2.0	0.3	8.5	CS03, HCOp04, HNC01, C2H03
CS15	16:20:09.6	-50:53:16.9	-60.1	2.4	1.4	1.4	2.0	0.6	8.6	CS05, HNC11
CS16	16:21:30.3	-50:26:52.9	-54.8	2.5	1.2	1.6	1.9	0.6	9.6	CS07, HCOp16, HCOp20, HNC12, C2H02
CS17	16:21:16.5	-50:39:40.9	-57.6	2.0	1.2	1.6	1.9	0.1	7.3	CS08, HCOp07, HNC07, C2H07
CS18	16:20:38.0	-50:41:34.9	-54.8	2.1	0.9	2.0	1.9	0.3	6.9	−
CS19	16:21:18.3	-50:30:34.9	-52.2	2.0	0.9	2.2	1.9	0.4	7.1	C2H13
CS20	16:21:13.3	-50:33:40.9	-51.5	2.1	1.1	2.0	1.8	0.4	8.3	HNC15

the parameters of the brightest 20 clumps of CS, HCO$^+$, HNC and C$_2$H emission according to their peak intensities, along with the derived luminosity in Table 3, 4, 5 and 6, respectively. A complete list of the clumps is available in the online version. The temperatures listed are corrected for the beam efficiency, $T_b = T_A^*/\eta_\nu$, where η_ν is the extended beam efficiency. For the twenty brightest clumps of each molecular species, we also listed their associated clumps in other molecules in the last column of the tables. The association criteria are: the clumps coincide within one beam and the line widths overlap. We have also plotted the clump positions on the corresponding integrated intensity map in Figures 6 and 7, with ellipses of size proportional to the angular sizes of the clumps. A summary of the clump properties is listed in Table 7 for comparison. The centroid velocities and line widths of the clumps among the four molecules are similar. The angular sizes of the clumps are also comparable among the four molecules, but note that the lower limit of angular size is just above the threshold value (1.5 beam-width) we have set.

4.2 Optical depth and column density

Among the four molecules decomposed by GAUSSCLUMPS, CS and HCO$^+$ have lines from rare isotopes, so-called 'iso-topologues' (C^{34}S and H^{13}CO$^+$) in our data set. Therefore it is possible to estimate optical depths for these molecules. Assuming identical excitation temperatures and optically thin emission from the rare isotopologues, the opacity τ relates to

Table 7. A summary of the clump properties for the CS, HCO$^+$, HNC and C$_2$H data cubes, derived from GAUSSCLUMPS (see Section 4).

|	CS	HCO$^+$	HNC	C$_2$H
Number of clumps	129	186	128	78
Centre velocity (km s^{-1})				
lowest	−61.9	−64.8	−65.9	−61.4
highest	−44.0	−44.4	−44.4	−43.5
mean	−52.0	−52.6	−52.6	−52.4
σ	4.1	3.8	3.7	3.5
Θ (arcmin)				
minimum	0.9	0.8	0.8	0.9
maximum	2.3	2.0	2.3	1.8
mean	1.4	1.4	1.3	1.3
σ	0.2	0.2	0.3	0.2
Peak T_b (K)				
minimum	0.7	0.7	0.7	0.5
maximum	7.6	5.4	4.4	1.8
mean	1.3	1.6	1.8	0.7
σ	1.0	0.7	0.7	0.3
dV (km s^{-1})				
minimum	0.4	0.5	0.4	0.3
maximum	4.1	3.8	3.7	3.2
mean	1.7	1.1	1.1	1.5
σ	0.7	0.6	0.6	0.6
Luminosity (K km s^{-1} pc^2)				
minimum	0.05	0.04	0.02	0.03
maximum	5.2	5.0	4.0	1.8
mean	0.6	0.4	0.5	0.2
σ	0.9	0.5	0.6	0.3
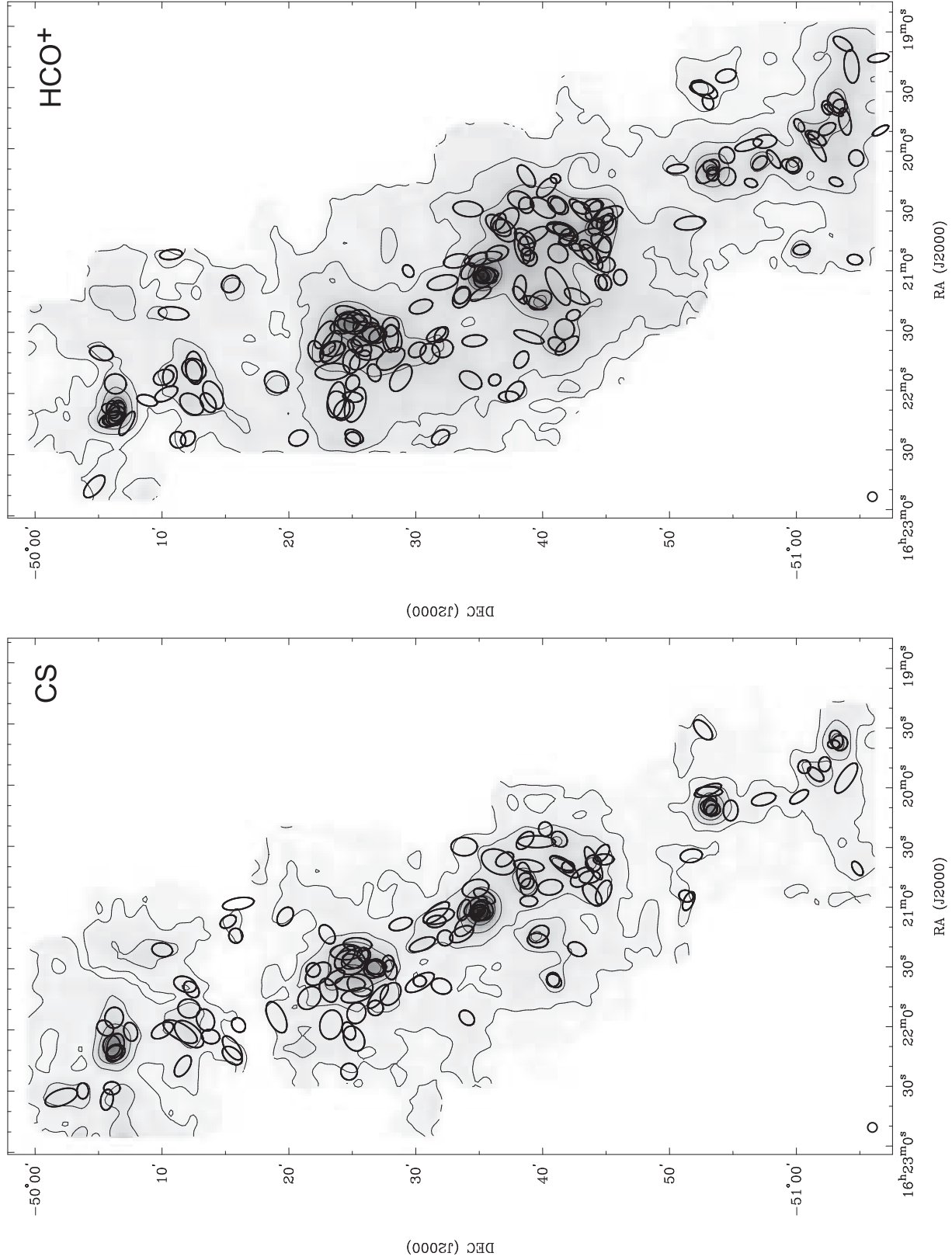
Figure 6. The integrated emission maps (contours and grey scale) of CS and HCO$^+$ (for the contour levels, see Figure 1) overlaid with the corresponding GAUSSCLUMPS clump fits of the 3-D data cube. The ellipses show the orientation and size of the clumps. Refer to Tables 3 and 4 for details of the clumps identified.
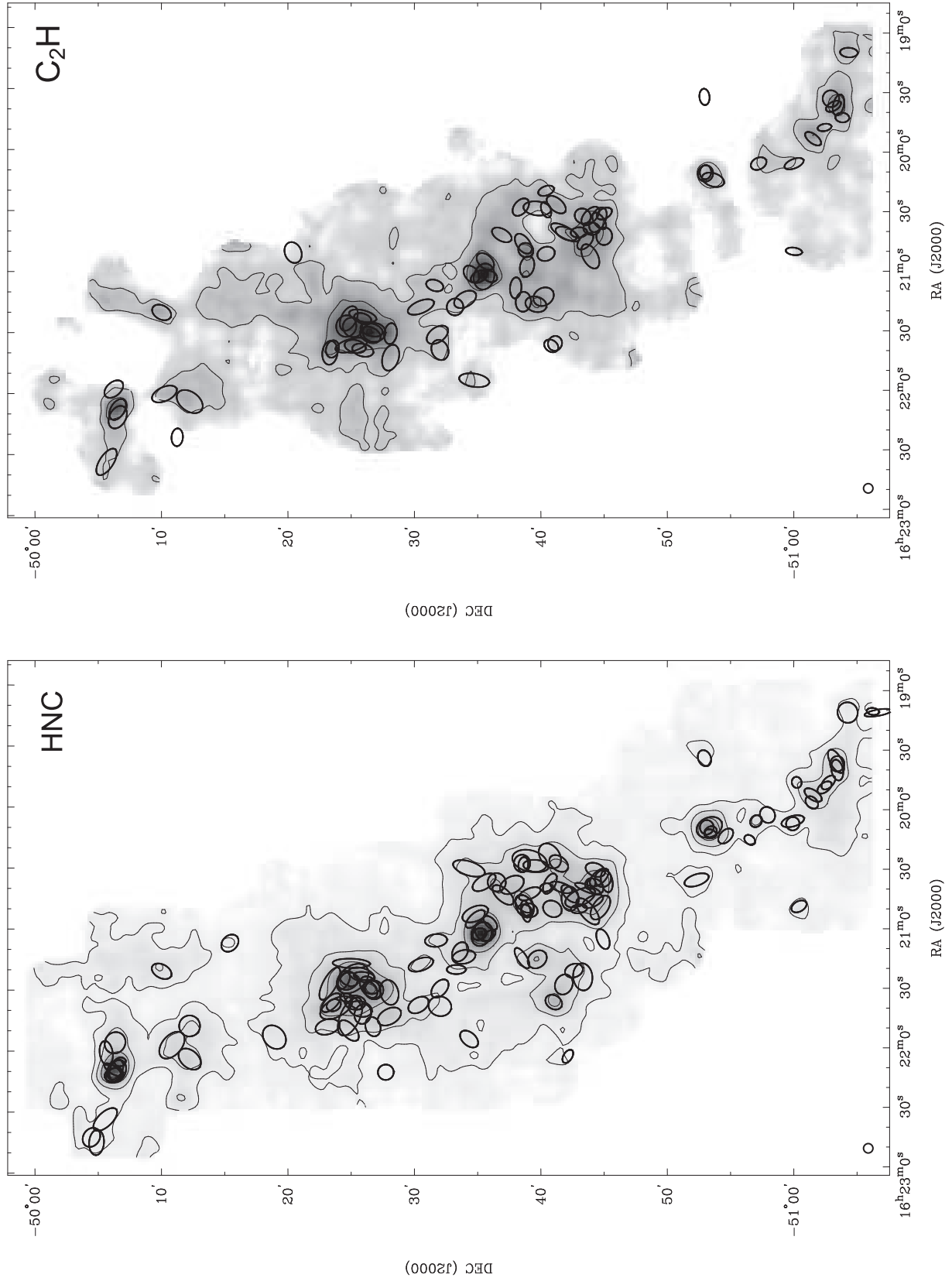
Figure 7. The integrated emission maps (contours and grey scale) of HNC and C$_2$H (for the contour levels, see Figure 2) overlaid with the corresponding GAUSSCLUMPS clump fits of the 3-D data cube. The ellipses show the orientation and size of the clumps. Refer to Tables 5 and 6 for details of the clumps identified.

Table 4. Same as Table 3 but for the 20 brightest HCO$^+$ clumps with peak temperatures above 5σ level of the Hanning smoothed data cube. The clumps are listed in descending peak T_b order. See the online version for a complete list of 186 clumps.

#	RA	Dec	v	ΔV	D_x	D_y	Peak T_b	dv/dr	L	Associated clumps in other molecules
HCOp01	16:22:08.5	-50:06:28.9	-49.1	2.4	1.7	1.1	5.4	0.6	23.8	CS03, HNC01, HNC10, C2H03
HCOp02	16:21:03.2	-50:35:28.9	-51.4	3.8	1.4	1.8	4.9	0.6	47.3	CS01, CS02, HNC02, C2H01
HCOp03	16:21:25.8	-50:24:40.9	-50.1	2.8	1.4	1.5	4.4	0.5	26.1	CS06, HNC03, C2H08
HCOp04	16:22:09.7	-50:06:22.9	-46.7	1.7	1.9	1.2	3.0	0.2	11.6	CS03, CS14, HNC01, C2H03
HCOp05	16:21:02.6	-50:35:10.9	-55.5	3.2	0.9	1.2	2.9	0.1	9.8	CS04, C2H05
HCOp06	16:20:05.8	-50:57:10.9	-56.0	2.0	1.1	1.4	2.9	0.6	8.5	HNC13, C2H20
HCOp07	16:21:14.6	-50:39:52.9	-56.0	3.1	1.5	1.9	2.9	0.8	23.6	CS08, CS17, HNC07, C2H07
HCOp08	16:21:40.3	-50:23:28.9	-50.8	1.9	1.4	2.1	2.6	0.3	13.8	HNC08
HCOp09	16:22:11.0	-50:06:28.9	-51.5	2.8	1.6	1.2	2.5	0.3	13.6	CS03, HCOp01, HNC10
HCOp10	16:20:38.1	-50:44:16.9	-53.1	2.4	1.2	1.4	2.3	0.4	8.4	HNC04, C2H10
HCOp11	16:20:44.4	-50:43:28.9	-60.5	1.7	1.6	2.9	2.1	0.2	15.1	HNC14
HCOp12	16:21:36.7	-50:41:10.9	-59.8	2.5	1.1	1.4	2.1	0.5	8.0	HNC09
HCOp13	16:20:39.3	-50:41:34.9	-54.6	2.0	1.0	1.4	2.0	0.6	5.1	CS18, C2H16
HCOp14	16:20:27.3	-50:41:16.9	-55.3	2.3	1.3	1.8	1.9	0.5	10.1	CS10, HNC16, C2H11
HCOp15	16:21:43.5	-50:28:04.9	-50.1	2.0	1.5	2.5	1.8	0.2	12.8	HNC20, C2H17
HCOp16	16:21:32.2	-50:27:04.9	-52.4	2.4	1.1	1.4	1.8	0.3	6.5	CS07, CS16, HNC12, C2H02
HCOp17	16:20:53.1	-50:43:58.9	-54.0	2.2	1.2	2.4	1.8	0.6	10.6	HNC19
HCOp18	16:20:11.5	-50:53:28.9	-54.4	2.6	1.2	1.1	1.8	0.4	5.7	CS05, CS09, HNC17
HCOp19	16:19:48.6	-51:02:28.9	-58.9	2.0	1.2	1.5	1.8	0.1	5.6	–
HCOp20	16:21:32.1	-50:26:22.9	-49.7	1.9	1.2	2.6	1.7	0.3	10.3	CS07, CS16, HNC12

Table 5. Same as Table 3 but for the 20 brightest HNC clumps with peak temperature above 5σ level of the Hanning smoothed data cube. The clumps are listed in descending T_b order. See the online version for a complete list of 128 clumps.

#	RA	Dec	v	ΔV	D_x	D_y	Peak T_b	dv/dr	L	Associated clumps in other molecules
HNC01	16:22:09.1	-50:06:22.9	-47.1	3.7	1.1	1.7	4.4	0.2	28.1	CS03, CS14, HCOp01, HCOp04, C2H03
HNC02	16:21:02.6	-50:35:22.9	-51.7	3.0	1.6	2.0	4.2	0.4	35.4	CS01, CS02, HCOp02, HNC05, C2H01
HNC03	16:21:25.8	-50:24:46.9	-50.4	2.9	1.3	1.6	3.4	0.5	19.8	CS06, HCOp03, C2H08
HNC04	16:20:38.7	-50:44:22.9	-52.7	2.4	1.2	1.4	2.9	0.5	10.9	HCOp10, C2H10
HNC05	16:21:01.3	-50:35:34.9	-49.2	2.1	1.4	1.7	2.8	0.2	13.2	CS02, HCOp02, HNC02, C2H01, C2H18
HNC06	16:21:02.6	-50:35:10.9	-54.6	2.6	0.9	1.2	2.8	0.1	7.4	CS04, HCOp02, HCOp05, HNC02, C2H05
HNC07	16:21:15.2	-50:39:46.9	-56.1	3.1	1.4	1.6	2.4	1.1	15.2	CS08, CS17, HCOp07, C2H07
HNC08	16:21:39.1	-50:23:52.9	-50.8	2.3	1.4	2.8	2.3	0.1	19.1	CS12, HCOp08, C2H15
HNC09	16:21:36.7	-50:41:04.9	-59.2	3.1	1.2	1.4	2.2	1.1	10.6	HCOp12
HNC10	16:22:09.7	-50:06:34.9	-49.7	2.8	1.8	1.3	2.2	0.3	12.9	CS03, HCOp01, HCOp09, C2H03
HNC11	16:20:08.9	-50:53:22.9	-58.1	3.3	1.9	2.1	2.1	0.6	25.7	CS05, CS15, C2H06
HNC12	16:21:30.3	-50:26:52.9	-52.1	3.0	1.5	1.5	2.1	0.3	12.6	CS07, CS16, HCOp16, HCOp20, C2H02
HNC13	16:20:05.8	-50:57:04.9	-56.1	2.0	1.1	1.0	2.0	0.6	4.3	HCOp06, C2H20
HNC14	16:20:44.4	-50:43:10.9	-60.5	1.7	1.4	2.5	1.9	0.1	10.7	HCOp11
HNC15	16:21:13.9	-50:33:58.9	-51.5	2.0	1.1	1.8	1.8	0.4	7.1	CS20
HNC16	16:20:27.3	-50:41:28.9	-56.1	2.3	1.2	1.7	1.8	0.2	7.9	CS10, HCOp14, C2H11
HNC17	16:20:11.5	-50:53:28.9	-54.6	2.9	1.1	1.1	1.8	0.5	5.6	CS05, CS09, HCOp18
HNC18	16:20:47.5	-50:38:46.9	-53.1	2.0	1.2	1.7	1.8	0.0	6.8	CS11, C2H04
HNC19	16:20:51.7	-50:43:46.9	-54.2	2.0	1.3	2.5	1.7	0.4	10.0	HCOp17
HNC20	16:21:43.5	-50:28:04.9	-50.3	1.9	1.2	2.0	1.6	0.1	6.9	HCOp15, C2H17

the brightness (beam efficiency corrected) of optically thick and thin emission lines as follows:

$$\frac{T_b(\text{thick})}{T_b(\text{thin})} = \frac{1 - e^{-\tau_{\text{thick}}}}{1 - e^{-\tau_{\text{thin}}}} = \frac{1 - e^{-\tau_{\text{thick}}}}{1 - e^{-\tau_{\text{thick}}/X}}, \quad (1)$$

where X is the abundance ratio, assuming $[\text{CS}/\text{C}^{34}\text{S}] = 22.5$ (Chin et al. 1996) and $[\text{HCO}^+/\text{H}^{13}\text{CO}^+] = 50$, based on $[\text{CO}/^{13}\text{CO}]$ from Wilson & Rood (1994).

After solving for τ, we next calculate the excitation tem-

perature T_{ex} from the optically thick emission lines, CS and HCO$^+$. From the equation of radiative transfer, T_{ex} can be derived from

$$T_b = f[J(T_{\text{ex}}) - J(T_{\text{bg}})][1 - e^{-\tau}]. \quad (2)$$

f is the beam filling factor which we assume to be 1, and $J(T) = T_0/(e^{T_0/T} - 1)$. Once τ and T_{ex} are known, the column density of the optically thick line can be derived

Table 6. Same as Table 3 but for the 20 brightest C$_2$H clumps with peak temperature above 3σ level of the Hanning smoothed data cube. The clumps are listed in descending peak T$_b$ order. See the online version for a complete list of 78 clumps. The C$_2$H clumps presented here refer to the main hyperfine component only, hence the luminosity is not calculated.

#	RA	Dec	v	ΔV	D_x	D_y	Peak T_b	dv/dr	Associated clumps in other molecules
C2H01	16:21:02.6	-50:35:34.9	-50.8	2.8	2.2	1.6	1.8	0.5	CS01, CS02, HCOp02, HNC02, HNC05, C2H18
C2H02	16:21:30.3	-50:26:52.9	-52.6	2.4	1.5	1.8	1.6	0.2	CS07, CS16, HCOp16, HNC12
C2H03	16:22:07.8	-50:06:34.9	-47.8	3.2	1.1	1.8	1.6	0.2	CS03, CS14, HCOp01, HCOp04, HNC01, HNC10
C2H04	16:20:49.4	-50:38:52.9	-53.7	2.1	1.2	1.2	1.4	0.3	CS11, HNC18
C2H05	16:21:02.6	-50:35:10.9	-54.0	2.1	0.9	1.4	1.3	0.3	CS04, HCOp02, HCOp05, HNC02, HNC06
C2H06	16:20:10.8	-50:53:04.9	-58.3	2.7	1.6	1.2	1.1	0.2	CS05, HNC11
C2H07	16:21:16.5	-50:39:40.9	-56.7	2.3	1.3	1.7	1.1	0.9	CS08, CS17, HCOp07, HNC07
C2H08	16:21:27.1	-50:24:40.9	-50.4	1.8	1.6	1.7	1.1	0.5	CS06, HCOp03, HNC03
C2H09	16:19:53.0	-51:01:34.9	-47.6	2.6	1.0	1.5	1.0	0.4	–
C2H10	16:20:38.7	-50:44:04.9	-52.6	2.0	1.1	1.3	1.0	0.7	HCOp10, HNC04
C2H11	16:20:26.7	-50:41:16.9	-55.5	2.4	1.1	1.8	1.0	0.5	CS10, HCOp14, HNC16
C2H12	16:19:35.8	-51:03:34.9	-50.1	2.5	1.2	1.7	1.0	0.2	CS13
C2H13	16:21:17.7	-50:30:34.9	-52.4	1.8	1.0	2.2	0.9	0.3	CS19
C2H14	16:22:04.1	-50:12:16.9	-49.7	2.0	1.5	2.3	0.9	0.4	–
C2H15	16:21:36.5	-50:25:04.9	-50.8	2.0	1.0	2.6	0.9	0.2	CS12, HNC08
C2H16	16:20:41.2	-50:42:04.9	-52.9	1.8	1.0	1.8	0.8	0.1	CS18, HCOp13
C2H17	16:21:42.9	-50:28:10.9	-50.5	1.4	1.3	2.1	0.8	0.3	HCOp15, HNC20
C2H18	16:21:02.6	-50:36:04.9	-48.8	1.3	0.9	1.1	0.8	0.3	CS05, CS09, HCOp02, HNC05
C2H19	16:21:20.0	-50:10:04.9	-43.5	1.9	1.1	1.6	0.8	0.1	–
C2H20	16:20:05.8	-50:57:16.9	-56.0	1.8	1.2	1.3	0.7	0.6	HCOp06, HNC13

with (cf Purcell et al. 2006)

$$N = \frac{8k\pi\nu^2}{hc^3 g_u A_{ul}} \frac{\tau}{1-e^{-\tau}} e^{-E_u/kT_{ex}} Q(T) \int T_b dv, \qquad (3)$$

where A_{ul} is the Einstein A coefficient in s^{-1}, ν is the transition frequency in Hz, $\int T_b dv$ is the integrated brightness temperature in K km s^{-1}, $Q(T)$ is the partition function, g_u is the upper state degeneracy and E_u is the upper state energy in m^{-1}. At positions, where no C^{34}S or H^{13}CO$^+$ was detected, we have assumed also that the main isotopologue was optically thin and the excitation temperature was set to 3 K. Eleven CS and two HCO$^+$ clumps fall into this category. The choice of 3 K for the excitation temperature was motivated by the median value of T_{ex} from clumps that show emission in the main and the rare species (Figures 10 and 11).

Shown in Figure 8 and 9 are histogram plots of CS and HCO$^+$ clump column density. The solid line shows the column density after correction for optical depth, and the dashed line shows the derived column density distribution by assuming CS and HCO$^+$ are optically thin with an excitation temperature of 20 K. The plots show that after correction, the column density increases by an order of magnitude. An examination of the clump spectra confirms that clumps with column density below 10^{13} cm^{-2} are those with minimal or no optically thin line detections, while those with column density of 10^{14} cm^{-2} or above are optically thick clumps.

An excitation temperature of 3 K is low. One possible cause could be due to the optically thin lines (C^{34}S and H^{13}CO$^+$) being spatially compact, and the assumption of having the same beam efficiency as the more common isotopologue may not hold. We thus also calculated the excitation temperatures of both CS and HCO$^+$ with
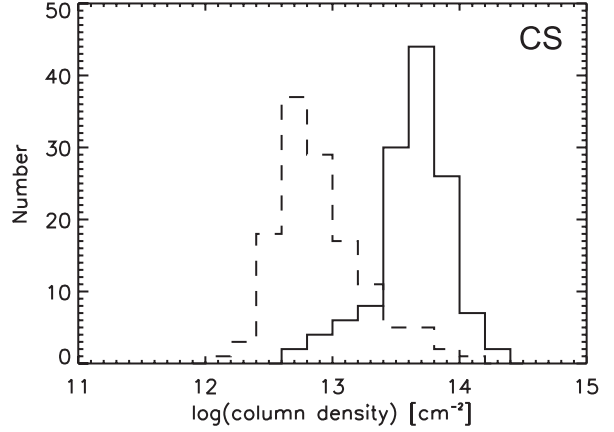

Figure 8. Histogram of CS clump column density with optical depth correction (solid). The dashed line shows the distribution obtained by assuming that CS is optically thin and has an excitation temperature of 20 K.

extended beam efficiency (η_{xb}) for CS and HCO$^+$, and main beam efficiency (η_{mb}) for C^{34}S and H^{13}CO$^+$. The excitation temperatures of CS and HCO$^+$ then increases to $\sim$4 K, still low. Another possibility is that the clumps are fragmented and unresolvable within the Mopra beam ($\sim$36 arcsec at 100-GHz). The clump finding algorithm sees these fragmented clumps as one single clump. Thus, the assumption of the beam filling factor (f) being unity does not hold, despite the fact that all identified clumps are larger than 1.5 beam widths. Various studies show that CS clumps are typically fragmented, with a volume filling factor as low as 0.2 (e.g. Stutzki & Guesten 1990; Juvela 1998). To investigate the effect of beam filling factor
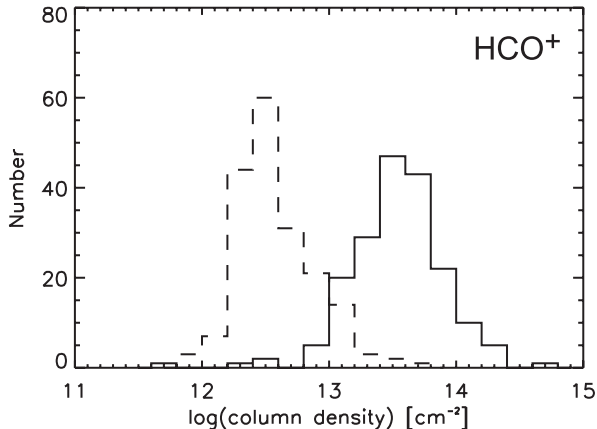
Figure 9. Histogram of HCO$^+$ clump column density with optical depth correction (solid). The dashed line shows the distribution obtained by assuming that HCO$^+$ is optically thin and has an excitation temperature of 20 K.
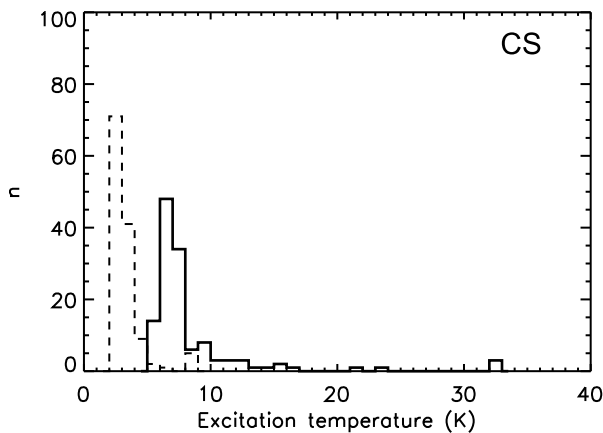

Figure 10. Histogram of CS clump excitation temperature with a beam filling factor of 0.2 (solid line). The dashed line shows the distribution assuming a unity beam filling factor.
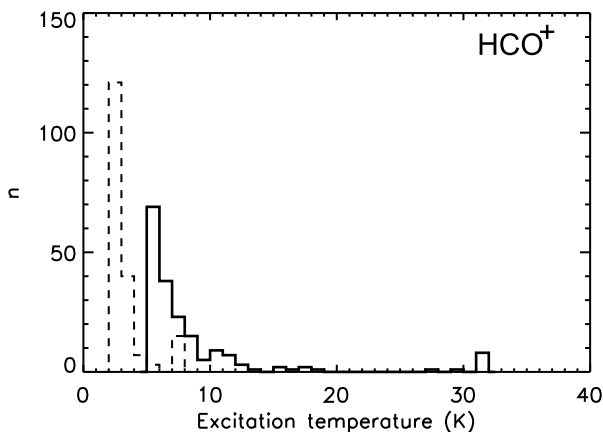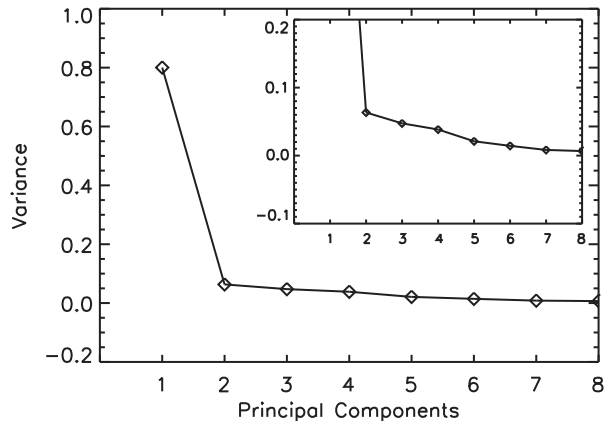

Figure 11. Histogram of HCO$^+$ clump excitation temperature with a beam filling factor of 0.2 (solid line). The dashed line shows the distribution assuming a unity beam filling factor.

Figure 12. Plot of variances of the principal components. The inset presents a zoomed version of the plot, showing the second and higher order components in more detail.

on the excitation temperature, we derived the excitation temperatures of CS and HCO$^+$ clumps with various beam filling factors. We found that with $f = 0.2$, approximately 74 per cent of the CS clumps, and 56 per cent of the HCO$^+$ clumps have T_{ex} between 6 to 20 K. Histograms of CS and HCO$^+$ excitation temperatures are shown in Figure 10 and 11 to illustrate the effect of lowering beam filling factor. The mean excitation temperature increases greatly by lowering the beam filling factor, suggesting the clumps may indeed fragmented and not resolvable with MOPRA beam. This would provide an explanation for the lack of correlation between clump size and line width (see Section 6.1 for details).

5   PRINCIPAL COMPONENT ANALYSIS

An alternative way to study the distribution of the molecules is by performing principal component analysis (PCA) on the integrated emission maps of the region. PCA is a multivariate data analysis technique, its purpose being to reduce the dimensionality of a data set. Mathematically the derivation of principal components involves finding the eigenvalues and eigenvectors of a covariance or correlation matrix (see e.g. Jolliffe 2002; Heyer & Schloerb 1997; Ungerechts et al. 1997, and references therein).

The purpose of performing PCA on the integrated emission maps is to characterise differences in molecular distribution. The G333 cloud consists of star forming sites at different stages of evolution, from cold dense starless cores to HII regions. Hence we expect to see chemical differences across the cloud. The data set covers varieties of chemical probes. Representative ones are the outflow tracer HCO$^+$, the large scale gas tracer ^{13}CO, the dense gas tracer CS, and the cold dense gas tracer N$_2$H$^+$. Interesting aspects are chemical differences and a possible temperature dependance of HCN to HNC abundance ratio. In this section, we will discuss the result of a PCA decomposition on the whole G333 molecular cloud; the PCA of individual regions of interest will be discussed in later sections.

We have chosen eight molecule lines with high signal-to-noise ratio for this analysis: ^{13}CO, C^{18}O, CS, HCO$^+$, HCN, HNC, N$_2$H$^+$ and C$_2$H (Figures 1 and 2). Among
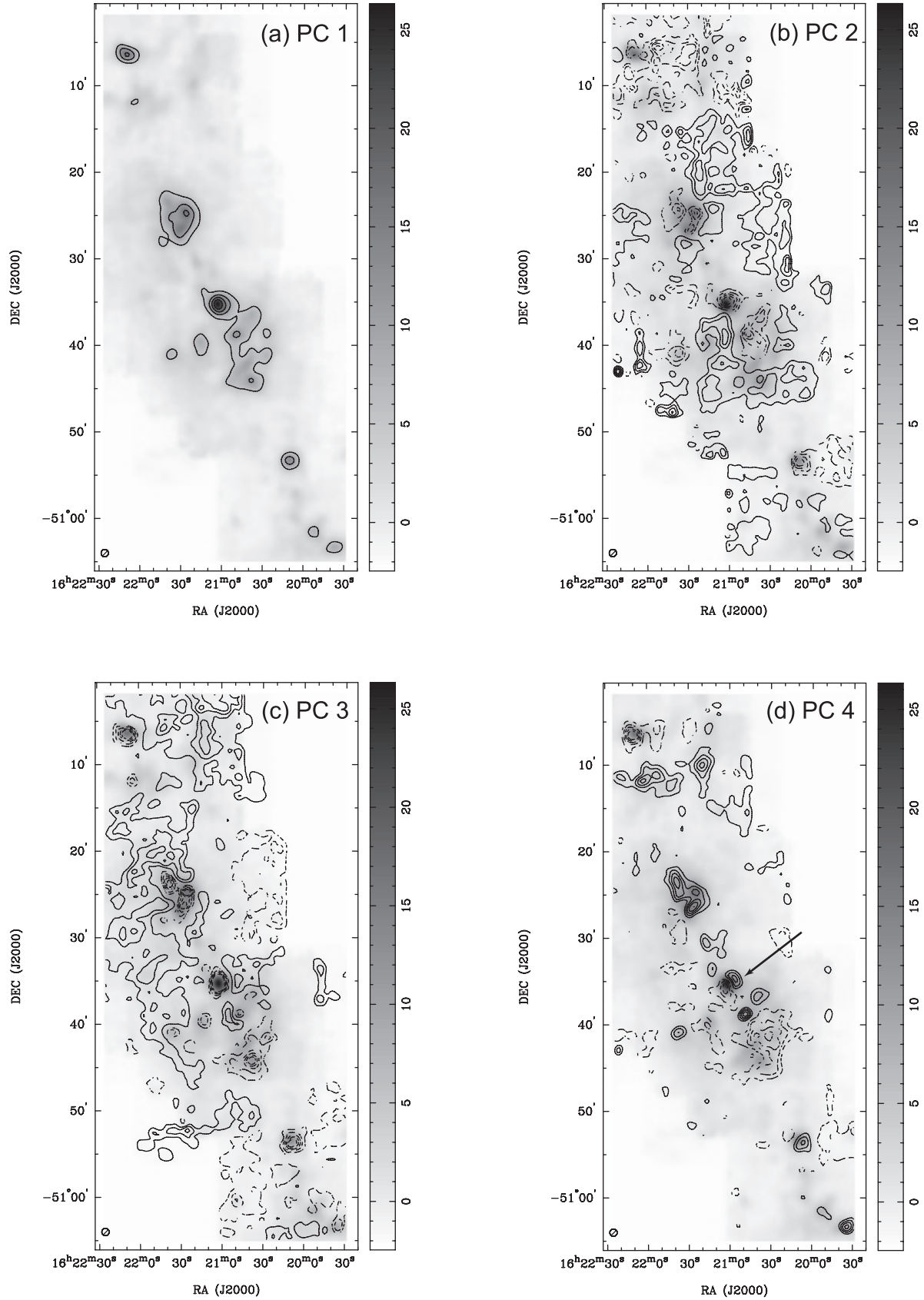
Figure 14. Constructed images of the first four principal components of the GMC. The contour levels are multiples of 20 per cent of the peak. The dashed contours represent an anti-correlation, while the solid contours represent a positive correlation in each of the principal components. The grey scale in each of the images shows the first principal component, overlaid with contours of the other principal components for ease of comparison. The lower left circles of each images indicate the beam size. The arrow indicates an example of anti-correlation between HCO^+ and N_2H^+ as discussed in Section 6.2.2.

Table 8. The correlation matrix of the input molecular data set for principal component analysis.

	CS	HCO$^+$	HNC	C^{18}O	C$_2$H	HCN	N$_2$H$^+$	^{13}CO
CS	1.00							
HCO$^+$	0.85	1.00						
HNC	0.90	0.92	1.00					
C^{18}O	0.77	0.80	0.81	1.00				
C$_2$H	0.60	0.70	0.67	0.61	1.00			
HCN	0.81	0.94	0.90	0.75	0.70	1.00		
N$_2$H$^+$	0.80	0.76	0.82	0.73	0.56	0.71	1.00	
^{13}CO	0.77	0.82	0.81	0.88	0.63	0.79	0.69	1.00

Table 9. The eigenvectors and eigenvalues of the principal components (PC) derived from the correlation matrix listed in Table 8.

	Percentage of variance	CS	HCO$^+$	HNC	C^{18}O	C$_2$H	HCN	N$_2$H$^+$	^{13}CO
PC 1	80.0	0.36	0.38	0.38	0.35	0.30	0.37	0.34	0.35
PC 2	6.3	-0.25	0.05	-0.10	-0.17	0.86	0.15	-0.36	-0.06
PC 3	4.7	-0.25	-0.11	-0.22	0.58	-0.07	-0.16	-0.38	0.61
PC 4	3.8	-0.05	-0.33	-0.17	0.21	0.38	-0.50	0.64	-0.03
PC 5	2.1	0.80	-0.26	0.07	-0.05	0.15	-0.34	-0.39	0.04
PC 6	1.4	0	0.03	0.13	0.68	0.01	0.02	-0.18	-0.70
PC 7	0.8	-0.25	-0.63	0.72	-0.03	0.01	0.13	-0.05	0.09
PC 8	0.7	0.22	-0.52	-0.48	0.10	-0.01	0.66	0.11	-0.03

these, C$_2$H has the lowest signal-to-noise level and ^{13}CO has the highest. The data sets were imported into IDL (a data visualisation and analysis platform) and each of their standard deviations were obtained. We decided to derive the principal components of the correlation matrix, rather than the covariance matrix. This is to avoid the principal components being dominated by a single variable (Jolliffe 2002, Chapter 3.3). An alternative approach involves normalising the data set first, and then deriving the principal components from the covariance matrix. We in fact derived the principal components using these two different approaches and obtained essentially the same result.

Listed in Table 8 is the correlation matrix of the input molecules, which describes how well the molecules correlate with each other. The correlation matrix shows there are four pairs of molecules which have correlation coefficients equal to or above 0.9. These are HCO$^+$ and HCN, HCO$^+$ and HNC, HCN and HNC, HNC and CS. This is consistent with the integrated intensity maps shown in Figure 1 and 2, where CS, HCO$^+$, HCN and HNC have similar large scale spatial distribution. However CS does show small differences in distribution, as discussed in Section 3.1. Among the eight molecules, C$_2$H and N$_2$H$^+$ have the lowest correlation coefficient. After forming the correlation matrix of the data set, we derived the eigenvalues and eigenvectors of the correlation matrix (Table 9). The eigenvalues indicate that the first principal component accounts for 80 per cent of total variation, while the first three principal components together account for over 90 per cent of total variation in the data set (see Table 9 and Figure 12). Figure 12 also shows that the first four principal components contain features above the noise level, while the variations contained in higher components are insignificant.

From the eigenvectors we constructed images of principal components (PC), by projecting the data set onto each of the eigenvectors. Shown in Figure 13 are plots of eigenvectors of each molecule in the first four principal components. A (negative) positive value indicates

the molecule is (anti-)correlated with others. The larger the value, the stronger the correlation. From the PC1 axis of Figure 13a it becomes clear that all of the eight molecules are positively correlated with each other. This can be visualised in Figure 14a, which is the whole data set projected onto the first principal component only. This also resembles an 'ideal' molecular distribution of the giant molecular cloud - the average intensity distribution of the species - and can be interpreted as the eight molecules being positively correlated on large scales. From the eigenvector plot of the second principal component (PC 2 axis of Figure 13a), C$_2$H stands out from other molecules; we suspect this is caused by scanning stripes resulting from the on-the-fly mapping procedure. This can be seen in the image of the second principal component (Figure 14b); note the vertical and horizontal stripes of solid contours which resemble the scanning patterns presented in the C$_2$H integrated emission map (Figure 2d). In fact, the scanning stripes are present in all data taken simultaneously as listed in Table 1 (the July, 2006 observation season). However, due to the lower signal-to-noise level of the C$_2$H emission, these scanning patterns become dominant in this map. We have explored the possibility of removing scanning artefacts by reconstructing the images without the second principal component. This indeed reduced the level of the artifacts, but it also subtracts a component of real emission from the image. Hence it provides a qualitative improvement, but the corrected image should not be used for quantitative studies.

From the eigenvector plot of the third principal component (Figure 13b) we can see C^{18}O and ^{13}CO are anti-correlated with other molecules. Spatially this anti-correlation appears as compact negative contours against a diffuse positive region in the third principal component image (Figure 14c). This could be due to the differences between high and low density tracers discussed in Section 6.2.1, with the CO isotopologue distribution being more extended.

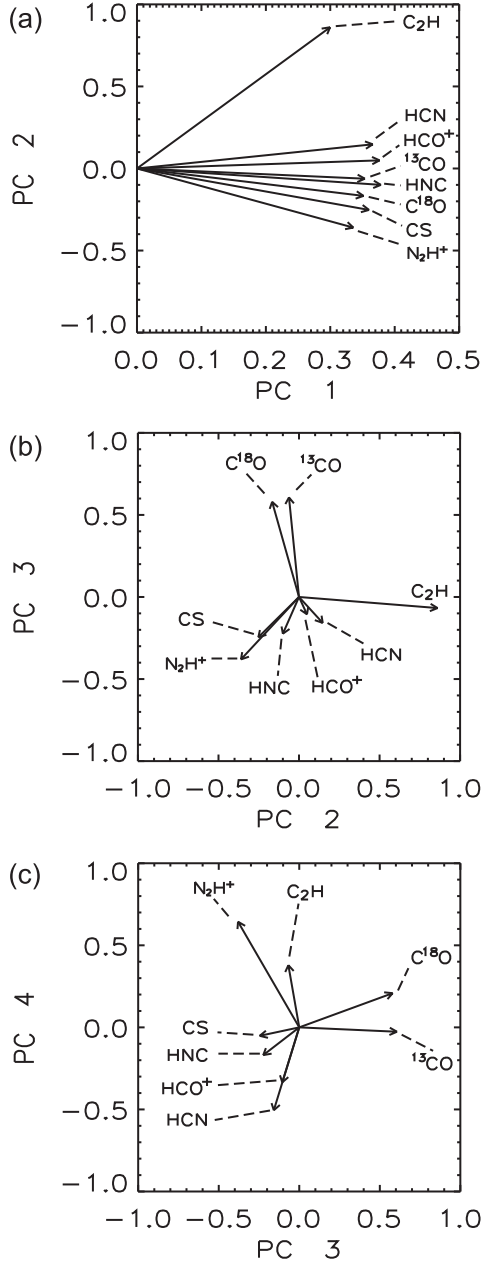The fourth principal component eigenvector plot

Figure 13. Plots of eigenvectors of the first three principal components of the data set. Each of the eigenvectors represent the component of that molecule in the relevant principal component.

(Figure 13c) shows an anti-correlation between N_2H^+ and HCO^+. The anti-correlation also appears clearly in the fourth principal component image (Figure 14d), notably across IRAS16172−5028 (shown by the arrow), possibly pointing to chemical differences across the object. Further discussion on this will be presented in Section 6.2.2.

The principal component analysis provides a way to quantify the spatial distribution of different molecules (with the constructed principal component images), and in placing different molecules into groups (with the eigenvectors). This results in minimising the number of different molecules required to characterise the basic properties of the cloud: CO isotopologues, HCO^+, N_2H^+, and C_2H. Implications

will be discussed in the next section.

6   DISCUSSION

In this section we discuss the results from this multi-molecular line survey and the analysis techniques applied. We also focus on particularly interesting regions in the G333 giant molecular cloud.

6.1   Size-line width, luminosity-size, and luminosity-line width correlation

To examine the correlation among the clump properties of CS, HCO^+ and HNC, we have compared luminosities of the molecular line emission, line widths and radii in Figure 15. The C_2H clumps presented here were obtained analysing the main hyperfine component only. Hence the entire line luminosity has not been calculated. The luminosity was calculated with

$$L = (d[pc])^2 (\frac{\pi}{180 \times 3600})^2 (r_x r_y) \int T dv, \quad (4)$$

where d is the distance to the GMC (3.6 kpc), r_x and r_y are the radii (arcsecond) of the two principal axes and $\int T dv$ (K km s^{-1}) is the sum of emission at the maximum position. We have discarded clumps with line widths below 0.7 km s^{-1}, as this is less than twice the effective spectral resolution of 0.3 km s^{-1} after hanning smoothing and binning the data. The slope of the ordinary least square (OLS) bisector (Feigelson & Babu 1992) line of best fit (γ), estimates the structural relationship between variables X and Y, without assuming whether Y depends on X or vice versa. Values inside the curly brackets are the slopes of OLS $(X|Y)$, which minimises the residuals in X, and OLS $(Y|X)$ which minimises the residuals in Y. The number of clumps (N) are shown on the top left corners of correlation plots.

Larson (1981) empirically showed, utilising data from several molecular cloud surveys, that the line width ΔV appears to scale with cloud size r, $\Delta V \propto r^\gamma$. The common value quoted for γ is $\sim 0.4 \pm 0.1$ (see Mac Low & Klessen 2004, and references therein). However, significant deviations have been reported (e.g. Loren 1989; Caselli & Myers 1995; Plume, Jaffe, Evans II, Martin-Pintado & Gomez-Gonzalez 1997). Consistent with our analysis of ^{13}CO and $C^{18}O$ line emission (WLB2008), we find no correlation between line width and radius for CS, HCO^+ and HNC clumps. The line width-size (note radius is given, not diameter) plots (Figure 15a-c) show a large scatter, hence the fitted slopes are poorly constrained. Note the large differences between OLS $(X|Y)$ and $(Y|X)$ slopes. Other line width-size relation studies (e.g. Schneider & Brooks 2004, and references therein) also found no line width-size relation, and suggested its possible dependance on clump identification procedure.

There is a clear correlation between luminosity and radius among CS, HCO^+ and HNC clumps. The fitted OLS bisector slopes γ (3.8 to 4.6) are slightly steeper than found for ^{13}CO and $C^{18}O$ (~ 3.0). Since luminosity
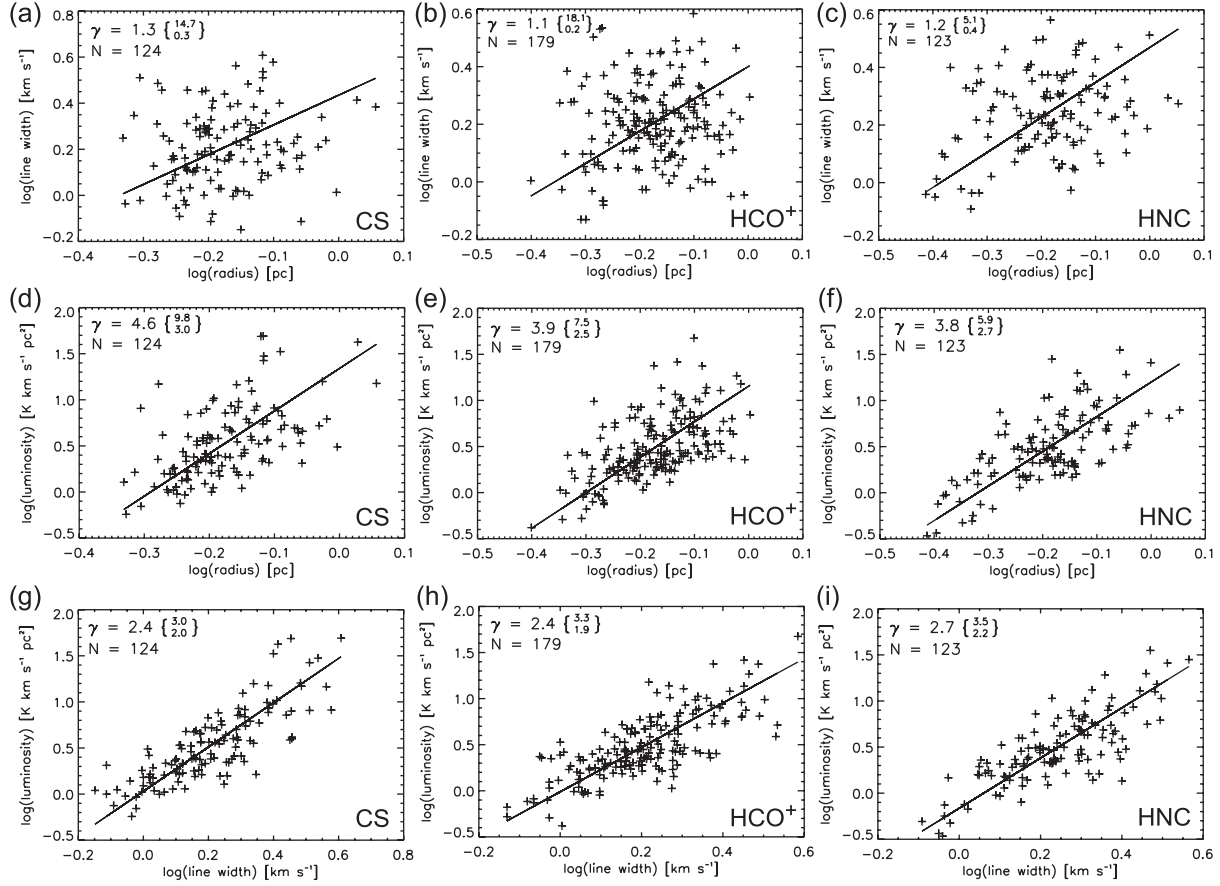
Figure 15. Plots of relationship between physical parameters for CS, HCO$^+$ and HNC clumps: (a) to (c) radius and line width; (d) to (f) luminosity and radius; (g) to (i) luminosity and line width. γ indicates the slope of the ordinary least square (OLS) bisector fitted solid line, the values in curly brackets are the slope of the OLS $(X|Y)$ and $(Y|X)$. N is the number of clumps. Note that clumps with line widths smaller than 0.7 kms $^{-1}$ are discarded.

implicitly depends on r^3, one would expect $\gamma \approx 3$, assuming a constant column density across the clumps. However, no statistical significance can be assigned to the value of slope, due to the inherent bias in clump finding algorithms, that tend to find larger clumps in denser regions (Schneider & Brooks 2004).

Similarly, luminosity and line width exhibits a strong correlation; this is not surprising as luminosity is calculated from the clump sizes and line widths. We do note that the ^{13}CO and C^{18}O clumps from previous work (WLB2008) were found using a different clump-finding algorithm, CPROPS.

6.2 Physical and chemical properties from PCA

In Section 5 we presented the results of principal component analysis, finding correlations or anti-correlations between molecular species. In the following sections, we discuss these in terms of the physical and chemical properties of the GMC.
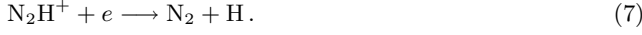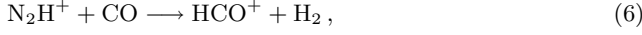
6.2.1 High and low density tracers

The eigenvector plot of the third principal component shows that ^{13}CO and C^{18}O are anti-correlated with the other molecules (Figure 13b); this can be visualised spatially from the projected principal component image as shown in Figure 14c. In this third PC image the compact dashed (negative) contours contrast spatially with the diffuse solid (positive) contours. This is due to C^{18}O and ^{13}CO ($J = 1 \rightarrow 0$) being low density tracers, and other molecules presented here being high density tracers (see Table 1 column 5). ^{13}CO and C^{18}O are present in both low and high density regions, whereas the other molecules are present in dense gas only. Hence in diffuse gas ^{13}CO and C^{18}O are in 'excess' compared to the high density tracers.

6.2.2 The anti-correlation of N_2H^+ and HCO^+

The eigenvector plot for the fourth principal component (Figure 13c) indicates the two ionic species N$_2$H$^+$ and HCO$^+$ are anti-correlated. According to models of dense clouds the major formation pathway of N$_2$H$^+$ is via ion-molecule reactions between N$_2$ and H$_3^+$ (Nejad, Williams & Charnley 1990). It is mainly destroyed by reactions with CO (Tafalla, Myers, Caselli & Walmsley 2004) and by recombi-

nation with electrons in hot regions (Sternberg & Dalgarno 1995). The following chemical equations summarise the mentioned reactions,

$$N_2 + H_3^+ \longrightarrow N_2H^+ + H_2 \,, \tag{5}$$

$$N_2H^+ + CO \longrightarrow HCO^+ + H_2 \,, \tag{6}$$

$$N_2H^+ + e \longrightarrow N_2 + H \,. \tag{7}$$

HCO^+ can be formed by ion-molecule reaction between N_2H^+ and CO (Equation 6), or between CO and H_3^+ (Sternberg & Dalgarno 1995) as shown in Equation 8 below,

$$CO + H_3^+ \longrightarrow HCO^+ + H_2 \,. \tag{8}$$

In cold dense cores, CO, the major destroyer of N_2H^+, will be depleted, so that the N_2H^+ abundance increases. With the lack of CO molecules, HCO^+ loses both of its major pathways (CO reacting with N_2H^+ or H_3^+), so the abundance of HCO^+ decreases. On the other hand, in warm regions where CO is not depleted, it reacts with N_2H^+ and produces HCO^+ causing a decrease in N_2H^+ and increase in HCO^+. CO reactions with H_3^+ further increase the HCO^+ abundance.

Prominent sites to study this phenomenon are located in the vincinity of HII regions, i.e. in photodissociation or photon dominated regions (PDRs), where at the cloud surface a high HCO^+ and a low N_2H^+ abundance is expected. In contrast, in the inner part of the cloud, where material is collapsing to form a dense core, CO is depleted causing an increase in N_2H^+ and a drop in HCO^+ abundance. Thus HCO^+ and N_2H^+ should be anti-correlated.

6.2.2.1 IRAS16172−5028
The HII region associated with IRAS16172−5028 provides a good candidate to test whether N_2H^+ and HCO^+ are anti-correlated. As suggested by the compact intense N_2H^+ emission, this source has a cold high density component, but is immersed in a strong PDR according to the bright 8.0-μm emission. To exclude the effects of large-scale spatial contamination, we applied PCA to the integrated emission map of this region. Listed in Table 10 are the eigenvalues and eigenvectors for this analysis; the eigenvectors of the second, third and fourth principal components are also plotted in Figure 16; where the anti-correlation of HCO^+ and N_2H^+ is clearly seen. In the eigenvector plot of the second and third principal components (Figure 16a), C_2H has the strongest positive correlation among the molecules. This is due to its spatially wide-spread emission towards the south-eastern region, compared to, for example, N_2H^+. Figure 17 shows the GLIMPSE 8.0-μm image (grey scale) overlaid with contours of the second principal component of the HII region associated with IRAS16172−5028, demonstrating that there are two regions with molecular emission that are anti-correlated. An examination of the eigenvectors shows that C_2H, HCO^+ (thick contours) and N_2H^+ (thin contours) contribute significantly to the variance in the second component and are anti-correlated, as expected for the hypothesis above. Note that the 8.0-μm emission (PAHs and warm gas) coincides well with the thick contours (HCO^+).

The second and third principal components of this region also show that ^{13}CO and $C^{18}O$ are correlated with
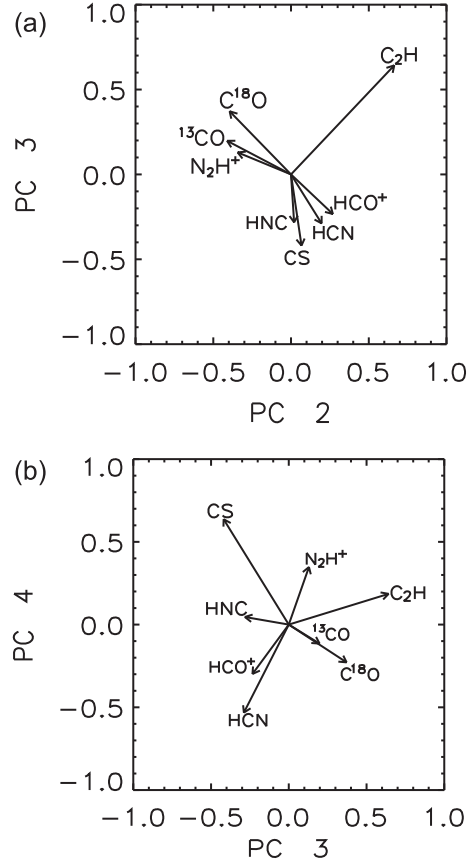
Figure 16. The eigenvectors of principal components two, three and four of the gas near the HII region associated with IRAS16172−5028.
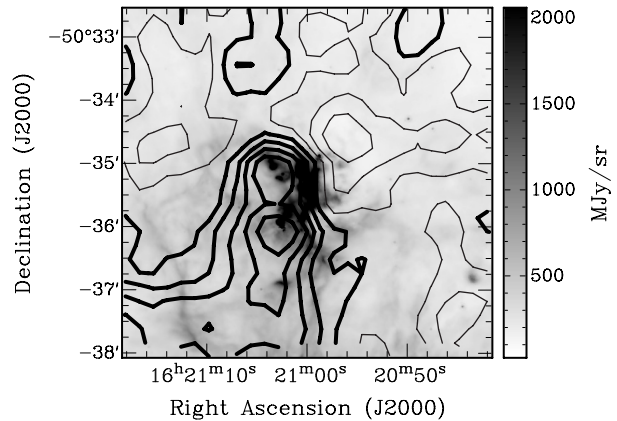
Figure 17. An image of the second principal component (contours) of the gas near the HII region associated with IRAS16172−5028 overlaid on the GLIMPSE 8.0-μm image (grey scale). The thin contours show regions with negative correlation to this component (mainly N_2H^+) and the thick contours are regions with positive correlation (mainly HCO^+).
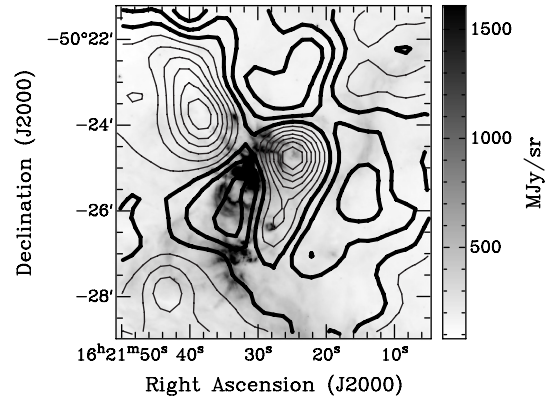
Table 10. The eigenvectors and eigenvalues of the principal components (PC) of the gas near the HII region associated with IRAS16172−5028.

	Percentage of variance	CS	HCO$^+$	HNC	C^{18}O	C$_2$H	HCN	N$_2$H$^+$	^{13}CO
PC 1	84.8	0.36	0.37	0.37	0.35	0.31	0.36	0.35	0.35
PC 2	6.7	0.07	0.27	0.02	-0.39	0.66	0.20	-0.34	-0.41
PC 3	3.4	-0.42	-0.23	-0.28	0.37	0.64	-0.29	0.13	0.20
PC 4	2.3	0.64	-0.30	0.05	-0.23	0.19	-0.53	0.35	-0.11
PC 5	1.4	0.35	-0.07	0.05	0.20	0.04	-0.21	-0.78	0.43
PC 6	0.6	0.17	-0.03	0.03	0.70	-0.06	-0.02	-0.11	-0.68
PC 7	0.4	-0.21	-0.63	0.72	-0.06	0.10	0.18	-0.08	-0.04
PC 8	0.3	-0.31	0.50	0.51	0	-0.05	-0.62	-0.02	-0.06

Table 11. The eigenvectors and eigenvalues of the principal components (PC) of the gas near the HII region associated with IRAS16177−5018.

	Percentage of variance	CS	HCO$^+$	HNC	C^{18}O	C$_2$H	HCN	N$_2$H$^+$	^{13}CO
PC 1	86.0	0.36	0.36	0.37	0.35	0.31	0.36	0.35	0.36
PC 2	5.4	-0.01	-0.08	0.08	-0.46	0.79	0.18	-0.09	-0.34
PC 3	3.0	0.04	-0.36	-0.19	0.45	0.40	-0.16	-0.53	0.41
PC 4	2.8	0.29	-0.43	-0.04	0.15	0.17	-0.54	0.61	-0.17
PC 5	1.1	-0.81	0.25	-0.14	0.21	0.27	-0.16	0.33	0.11
PC 6	0.7	-0.30	-0.70	0.24	-0.02	-0.14	0.52	0.22	0.16
PC 7	0.6	-0.01	0	-0.12	0.62	-0.01	0.31	-0.07	-0.71
PC 8	0.4	-0.18	-0.01	0.85	0.12	-0.04	-0.36	-0.26	-0.17
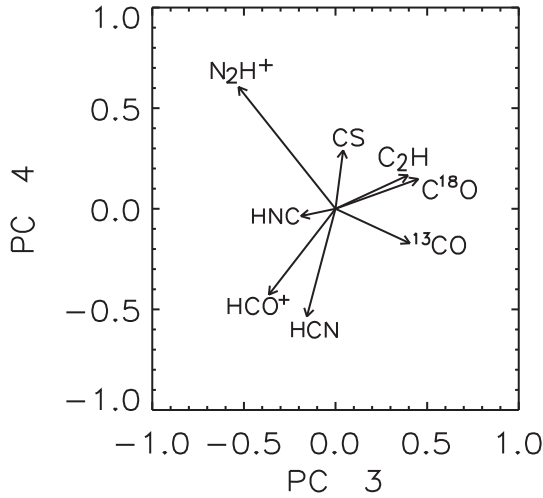
Figure 18. The eigenvectors of principal components two, three and four of the gas near the HII region associated with IRAS16177−5018.

Figure 19. An image of the third principal component (contours) of the gas near the HII region associated with IRAS16177−5018 overlaid on the GLIMPSE 8.0-μm image (grey scale). The thin contours showing regions with negative correlations (mainly N$_2$H$^+$) and the thick contours are regions with positive correlations (mainly ^{13}CO and C^{18}O).

N$_2$H$^+$ (Figure 16a), which contradicts the idea suggesting that CO is the main destroyer of N$_2$H$^+$. However, we believe this can be explained by considering the different density conditions that these two species are tracing. CO is a low density tracer having a critical density of $\sim 10^3$ cm^{-3}, while N$_2$H$^+$ is a high density tracer with a critical density of $\sim 10^5$ cm^{-3}. Therefore CO is tracing both low and high density gas along the line of sight. Since maps of integrated emission were used for the PCA, the ^{13}CO and C^{18}O may arise from a molecular envelope almost devoid of N$_2$H$^+$, while the bulk of the N$_2$H$^+$ emission is arising from the core.

6.2.2.2 IRAS16177−5018 Another example is the molecular emission associated with IRAS16177−5018 as

shown in Figures 19 and 20. The eigenvalues and eigenvectors of the principal components are listed in Table 11, while the eigenvectors of the third and fourth principal components are plotted in Figure 18. Similar to the other source IRAS16172−5028, this region also shows an anti-correlation of N$_2$H$^+$ and HCO$^+$ in the fourth principal component (Figure 20). On the other hand, shown in the third principal component (Figure 19) is an anti-correlation of N$_2$H$^+$ and CO isotopologues.

The PCA also indicates that HCN and HCO$^+$ are correlated, as shown in the eigenvector plots of the entire
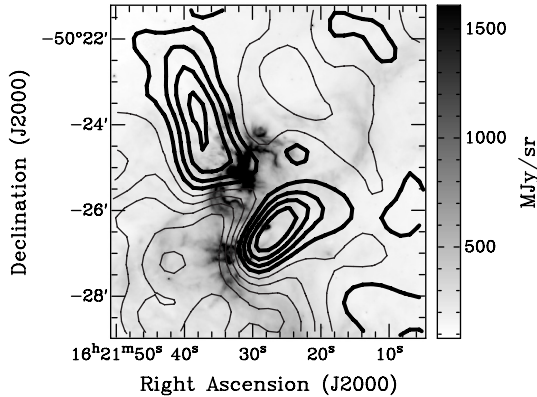
Figure 20. Similar to Figure 19 but the fourth principal component (contours) overlaid on the GLIMPSE 8.0-μm image (grey scale). The thin contours show regions with negative correlation to this component (mainly HCO$^+$) and the thick contours are regions with positive correlation (mainly N$_2$H$^+$).

region (Figure 13). This correlation has also been suggested by other studies, such as by Turner & Thaddeus (1977) for Orion-KL. IRAS16172$-$5028 and IRAS16177$-$5018 are both known to be associated with an H II region, contain cold molecular gas of high density (bright compact N$_2$H$^+$ emission), and have a low photon exposure. As expected by chemical models, both sources clearly show that N$_2$H$^+$ and HCO$^+$ are anti-correlated.

6.3   The infrared ring

Another note worthy feature in G333 is a ring of mid-infrared emission as shown in Figure 21, the northern portion of which is aligned with an arc of N$_2$H$^+$ emission (see the top arrow on Figure 2). This ring feature is visible in the GLIMPSE 5.8 and 8.0-μm (Figure 21 top right and bottom left panels) images, but is marginally detectable in 3.6- (Figure 21 top left panel) and 4.5-μm images. The GLIMPSE 5.8 and 8.0-μm channels of the *Spitzer* IRAC instrument are dominated by PAH emission excited by nearby ultraviolet sources (Reach et al. 2006). Lying inside the emission ring but offset towards the edge, is bright MIPS-GAL (Carey et al. 2006) 24-μm emission (Figure 21 bottom right panel), spatially coincident with the *MSX* point source G333.5114$-$00.2798 (marked with a white circle; Egan et al. 2003) and an *IRAS* source IRAS16182$-$5005 (marked with triangle). The absence of the emission ring at 24-μm further suggests that the emission originates from PAHs, and that there is a lack of thermal dust emission.

Comparing the MIPSGAL 24-μm emission with the 843-MHz radio continuum (Figure 21d contours) from the Molonglo Galactic Plane Survey (MGPS, Green et al. 1999), it is clear that the radio continuum is associated with the 24-μm emission. A search of the SIMBAD astronomical

database and VizieR catalogue service[3] did not lead to the identification of any supernova or X-ray source, suggesting there is an H II region inside the 8-μm emission ring. Shown in Figure 21b is the 5.6-μm emission ring (grey scale) overlaid with 1.2-mm dust continuum contours (Mookerjea et al. 2004); the 1.2-mm dust continuum lies next to the bright 8-μm rim and is coincident with a dark filament (appearing white in the grey scale image). According to Mookerjea et al. (2004), this source (MMS16) has a density of $\sim 2 \times 10^4$ cm^{-3}. The 1.2-mm dust continuum emission agrees well with the arc of N$_2$H$^+$ emission (Figure 21c) described above. There is no detectable dust continuum from the south-western region of the ring. Molecular emission is detected from this part but it is weak and diffuse, indicating a relative low density region compared to the dust. Given the completeness and symmetry of the ring, one might expect the H II region to lie near the centre. Since it does not, we suggest the possibility that this is due to density differences in the gas surrounding the infrared ring. In general H II regions are density bounded, and the pressurised H II gas breaks out of the cloud into lower-density gas, creating a champagne flow (Stahler & Palla 2005). The inhomogeneous density (from our molecular line data) allows the ionised gas to spread out further towards the south-west compared to the north-east rim, creating a near circular 8-μm emission structure with the driving source lying on the edge. However the extreme symmetry also suggests the ring could be a pre-existing structure that is currently being illuminated by the H II region. In either way this infrared emission ring must be related to the H II region.

Another notable feature is the spatial coincidence of mm dust continuum, N$_2$H$^+$ emission and the infrared dark filament (which appears as white in the grey scale image) to the north of the ring (Figure 21b and c). As CO is frozen on to grains in dense cold gas (see e.g. Kramer et al. 1999; Bacmann et al. 2002), causing it to be depleted, and the ion-molecule formation reaction for N$_2$H$^+$ proceeds regardless of temperature, N$_2$H$^+$ is a good candidate for tracing cold dense gas where CO is depleted. With mm dust continuum tracing cold dust along with N$_2$H$^+$ tracing cold dense gas, it is not surprising that they coincide with the infrared dark filament.

7   SUMMARY

In this paper we have presented data from a multi-molecular line survey of the southern star forming region, the G333 giant molecular cloud complex. For this survey, we have exploited the Mopra MMIC receiver and the 8-GHz bandwidth UNSW-Mopra Spectrometer, resulting in over twenty multi-molecular transition maps, with velocity resolution of ~ 0.1 km s^{-1}. We have presented total intensity maps of molecules with bright emission and have also discussed the velocity structure of the G333 molecular cloud. To further characterise the physical and chemical properties, we have carried out common analysis techniques such as GAUSSCLUMPS to obtain distributions of CS, HCO$^+$, HNC and C$_2$H emission. We have also performed principal component analysis on
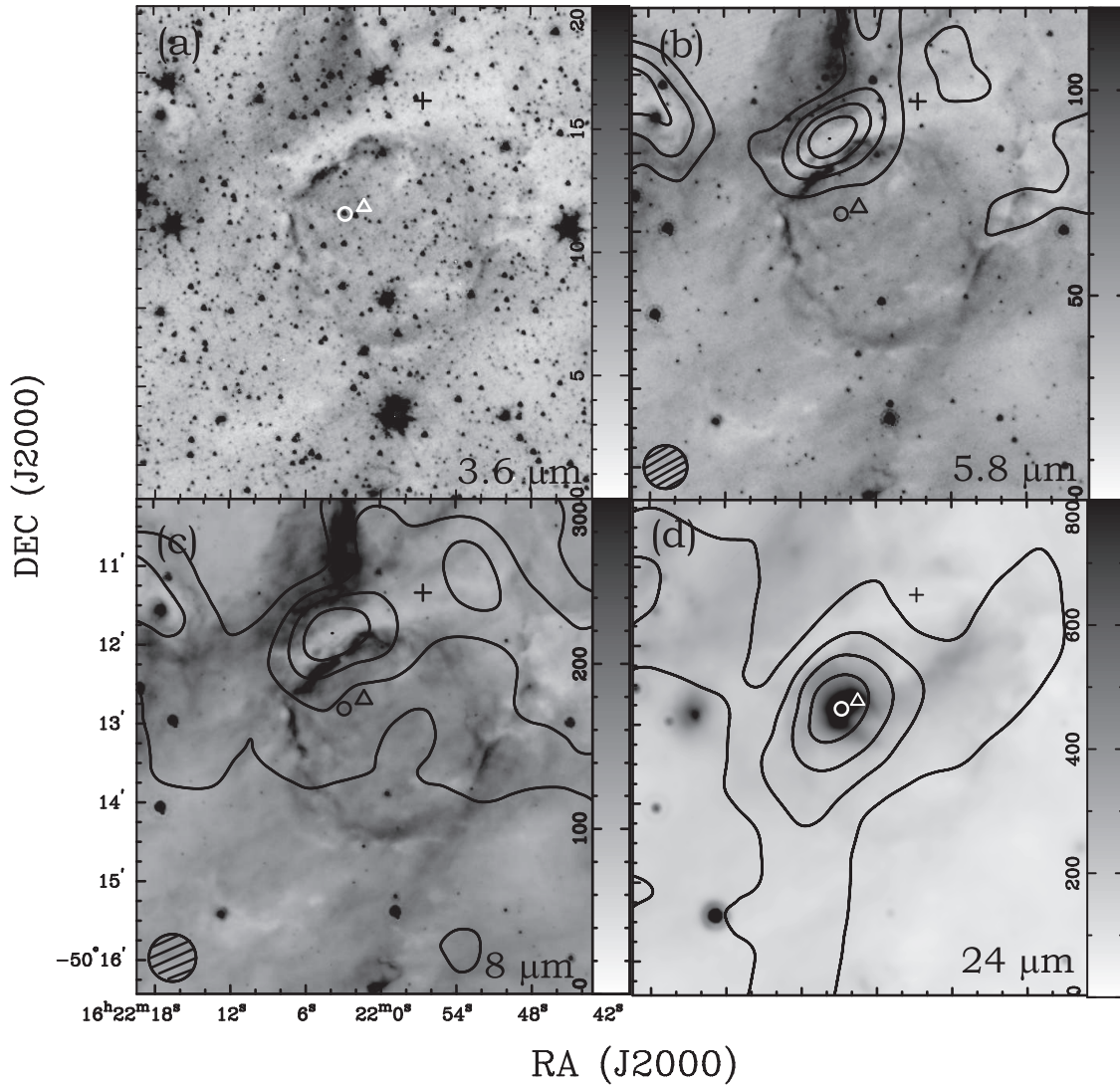
---

[3] http://cdsweb.u-strasbg.fr/

Figure 21. (a) GLIMPSE 3.6-μm image; (b) GLIMPSE 5.8-μm image overlaid with 1.2-mm dust continuum contours (Mookerjea et al. 2004); (c) GLIMPSE 8.0-μm images overlaid with N_2H^+ integrated emission contours and (d) MIPSGAL 24-μm image overlaid with MGPS 843-MHz radio continuum contours of the infrared ring discussed in Section 6.3. The grey scale is stretched to 0 - 20 MJy sr^{-1} for the GLIMPSE 3.6-μm, 0 - 120 MJy sr^{-1} for the 5.8-μm image, 0 - 300 MJy sr^{-1} for the 8-μm image and 0 - 800 MJy sr^{-1} for the MIPSGAL image. The contours are at multiples of 20 per cent level of each of the emission peaks. The hatched circles represent the beam size of the respective contour maps. The small circle indicates the position of the *MSX* point source G333.5114-00.2798, the triangle marks the position of the *IRAS* source, IRAS16182−5005 (resolution of $\sim$ 4 arcmin) and the cross shows the position of a far-infrared source (Karnik et al. 2001, resolution of $\sim$ 1 arcmin) which peaks at 100-μm. Note the ring feature present at 5.8 and 8.0-μm, which is dominated by PAHs, the bright 24-μm emission which lies inside this ring. Both the 1.2-mm dust continuum and the integrated N_2H^+ emission coincide with the infrared dark filaments, which appear white in the 5.8 and 8.0-μm grey scale images.

the data set, to visualise and parameterise the differences between the spatial distribution of molecules. In this work, we have found:

(i) Differences in spatial and velocity distribution among different molecules. We found that the spatial distribution of CS, HCO$^+$, HCN and HNC are similar on large scales, while N_2H^+ seems to trace preferentially the very densest regions. C_2H is only detected close to bright infrared emission regions. The detected molecules all have similar velocity distributions.

(ii) The velocity gradient across the GMC complex noted

in ^{13}CO (BWC2006) and C^{18}O (WLB2008) is also present in CS, HCO$^+$ and HNC.

(iii) CS, HCO$^+$ and HNC emission maps were decomposed with GAUSSCLUMPS in three dimensions. We found no correlation between clump radius and line width, but a clear correlation between luminosity and radius. Accounting for saturation effects in the CS ($J = 2 \rightarrow 1$) and HCO$^+$ ($J = 1 \rightarrow 0$) lines toward clumps, we obtain column densities of $\sim 10^{12}$ to $\sim 10^{14}$ cm^{-2}.

(iv) An alternative approach used to characterise this data set was principal component analysis (PCA). PCA separates molecules into low (^{13}CO and C^{18}O) and high (the rest) density tracers, identifies anti-correlations be-

tween HCO^+ and N_2H^+, correlations between HCN and HCO^+, and helps to explore scanning patterns of the 'on-the-fly' mapping.

(v) A noteworthy 'ring-like' structure of the GMC is present in the GLIMPSE 8-μm image, associated with an HII region as suggested by radio continuum emission inside the ring. The molecular line data (especially N_2H^+) shows gas being swept up and compressed by the ring.

ACKNOWLEDGMENTS

REFERENCES

Bacmann A., Lefloch B., Ceccarelli C., Castets A., Steinacker J., Loinard L., 2002, A&A, 389, L6

Bains I., Wong T., Cunningham M., Sparks P., Brisbin D., Calisse P., Dempsey J. T., Deragopian G., et al., 2006, MNRAS, 367, 1609

Becklin E. E., Frogel J. A., Neugebauer G., Persson S. E., Wynn-Williams C. G., 1973, ApJ L, 182, L125+

Benjamin R. A., Churchwell E., Babler B. L., Bania T. M., Clemens D. P., Cohen M., Dickey J. M., Indebetouw R., et al., 2003, PASP, 115, 953

Breen S. L., Ellingsen S. P., Johnston-Hollitt M., Wotherspoon S., Bains I., Burton M. G., Cunningham M., Lo N., Senkbeil C. E., Wong T., 2007, MNRAS, 377, 491

Carey S. J., Noriega-Crespo A., Mizuno D. R., Shenoy S., Paladini R., Kraemer K. E., Kuchar T. A., Marleau F. R., et al., 2006, 38, 1023

Caselli P., Myers P. C., 1995, ApJ, 446, 665

Chin Y.-N., Henkel C., Whiteoak J. B., Langer N., Churchwell E. B., 1996, A&A, 305, 960

Colgan S. W. J., Haas M. R., Erickson E. F., Rubin R. H., Simpson J. P., Russell R. W., 1993, ApJ, 413, 237

Egan M. P., Price S. D., Kraemer K. E., 2003, 35, 1301

Feigelson E. D., Babu G. J., 1992, ApJ, 397, 55

Fujiyoshi T., Smith C. H., Caswell J. L., Moore T. J. T., Lumsden S. L., Aitken D. K., Roche P. F., 2006, MNRAS, 368, 1843

Fujiyoshi T., Smith C. H., Moore T. J. T., Aitken D. K., Roche P. F., Quinn D. E., 1998, MNRAS, 296, 225

Fujiyoshi T., Smith C. H., Moore T. J. T., Lumsden S. L., Aitken D. K., Roche P. F., 2005, MNRAS, 356, 801

Fujiyoshi T., Smith C. H., Wright C. M., Moore T. J. T., Aitken D. K., Roche P. F., 2001, MNRAS, 327, 233

Goss W. M., Shaver P. A., 1970, Australian Journal of Physics Astrophysical Supplement, 14, 1

Green A. J., Cram L. E., Large M. I., Ye T., 1999, ApJS, 122, 207

Heyer M. H., Schloerb F. P., 1997, ApJ, 475, 173

Hirota T., Yamamoto S., Mikami H., Ohishi M., 1998, ApJ, 503, 717

Jolliffe I., 2002, Principal Component Analysis. Springer

Jones P. A., Burton M. G., Cunningham M. R., Menten K. M., Schilke P., Belloche A., Leurini S., Ott J., Walsh A. J., 2008, MNRAS, 386, 117

Juvela M., 1998, A&A, 329, 659

Karnik A. D., Ghosh S. K., Rengarajan T. N., Verma R. P., 2001, MNRAS, 326, 293

Kramer C., Alves J., Lada C. J., Lada E. A., Sievers A., Ungerechts H., Walmsley C. M., 1999, A&A, 342, 257

Kramer C., Stutzki J., Rohrig R., Corneliussen U., 1998, A&A, 329, 249

Ladd N., Purcell C., Wong T., Robertson S., 2005, Publications of the Astronomical Society of Australia, 22, 62

Larson R. B., 1981, MNRAS, 194, 809

Lo N., Cunningham M., Bains I., Burton M. G., Garay G., 2007, MNRAS, 381, L30

Lockman F. J., 1979, ApJ, 232, 761

Loren R. B., 1989, ApJ, 338, 925

Lovas F. J., Johnson D. R., Snyder L. E., 1979, ApJ Supp, 41, 451

Mac Low M.-M., Klessen R. S., 2004, Reviews of Modern Physics, 76, 125

Mookerjea B., Kramer C., Nielbock M., Nyman L.-Å., 2004, A&A, 426, 119

Müller H. S. P., Schlöder F., Stutzki J., Winnewisser G., 2005, J. Molecular Structure, 742, 215

Müller H. S. P., Thorwirth S., Roth D. A., Winnewisser G., 2001, A&A, 370, L49

Nejad L. A. M., Williams D. A., Charnley S. B., 1990, MNRAS, 246, 183

Plume R., Jaffe D. T., Evans II N. J., Martin-Pintado J., Gomez-Gonzalez J., 1997, ApJ, 476, 730

Purcell C. R., Balasubramanyam R., Burton M. G., Walsh A. J., Minier V., Hunt-Cunningham M. R., Kedziora-Chudczer L. L., Longmore S. N., et al., 2006, MNRAS, 367, 553

Reach W. T., Rho J., Tappe A., Pannuti T. G., Brogan C. L., Churchwell E. B., Meade M. R., Babler B., Indebetouw R., Whitney B. A., 2006, ApJ, 131, 1479

Rodgers A. W., Campbell C. T., Whiteoak J. B., 1960, MNRAS, 121, 103

Rosolowsky E., Leroy A., 2006, PASP, 118, 590

Russeil D., Adami C., Amram P., Le Coarer E., Georgelin Y. M., Marcelin M., Parker Q., 2005, A&A, 429, 497

Schilke P., Walmsley C. M., Pineau Des Forets G., Roueff E., Flower D. R., Guilloteau S., 1992, A&A, 256, 595

Schneider N., Brooks K., 2004, Publications of the Astronomical Society of Australia, 21, 290

Sheth K., Vogel S. N., Wilson C. D., Dame T. M., 2008, ApJ, 675, 330

Stahler S. W., Palla F., 2005, The Formation of Stars. The Formation of Stars, by Steven W. Stahler, Francesco Palla, pp. 865. ISBN 3-527-40559-3. Wiley-VCH , January 2005.

Sternberg A., Dalgarno A., 1995, ApJS, 99, 565

Storey J. W. V., Harnett J. I., Lugten J. B., Crawford M. K., Stacey G. J., Watson D. M., Genzel R., 1989, MN-RAS, 237, 1001

Stutzki J., Guesten R., 1990, ApJ, 356, 513

Tafalla M., Myers P. C., Caselli P., Walmsley C. M., 2004, A&A, 416, 191

Turner B. E., Thaddeus P., 1977, ApJ, 211, 755

Ungerechts H., Bergin E. A., Goldsmith P. F., Irvine W. M., Schloerb F. P., Snell R. L., 1997, ApJ, 482, 245

Walsh A. J., Lo N., Burton M. G., White G. L., Purcell C. R., Longmore S. N., Phillips C. J., Brooks K. J., 2008, Publications of the Astronomical Society of Australia, 25, 105

Williams J. P., de Geus E. J., Blitz L., 1994, ApJ, 428, 693

Wilson T. L., Rood R., 1994, ARA&A, 32, 191

Wong T., Ladd E. F., Brisbin D., Burton M. G., Bains I., Cunningham M. R., Lo N., Jones P. A., Thomas K. L., Longmore S. N., Vigan A., Mookerjea B., Kramer C., Fukui Y., Kawamura A., 2008, MNRAS, 386, 1069

This paper has been typeset from a T_EX/ L^AT_EX file prepared by the author.